Challenge Journal of STRUCTURAL MECHANICS

Vol.3 No.2 (2017)

North Anatolian Fault Zone Poisson method building codes columns continuous girder bridge corrosion durability dynamic analysis dynamic response earthquake earthquake hazard finite element analysis finite element method optimization reinforced concrete seismic analysis seismic design seismic isolation seismic response teaching-learning based optimization wind

TULPAR ACADEMIC PUBLISHING

ISSN 2149-8024

Challenge Journal of Structural Mechanics

E-mail: *cjsmec@challengejournal.com*

Web page: *cjsmec.challengejournal.com*

TULPAR Academic Publishing
www.tulparpublishing.com

Challenge Journal of Structural Mechanics

CONTENTS

TULPAR ACADEMIC PUBLISHING

Challenge Journal of Structural Mechanics

Modal response identification of a highway bridge under traffic loads using frequency domain decomposition (FDD)

Mehmet Akköse [a,*], Hugo C. Gomez [b], Maria Q. Feng [c]

[a] *Karadeniz Technical University, Department of Civil Engineering, 61080 Trabzon, Turkey*
[b] *Holmes Culley, 235 Montgomery Street, Suite 1250, San Francisco, CA 94104, USA*
[c] *Department of Civil Engineering and Engineering Mechanics, Columbia University, New York, NY 10027, USA*

ABSTRACT

In this study, a four-span, 224m long, post-tensioned concrete box girder bridge supported on single column piers was subject to a series of controlled vehicle tests. Bridge acceleration response datasets were used to study the effect of truck speed and a sudden stop, on the modal identification of the bridge structure. Natural frequencies and mode shapes of the bridge were determined using the frequency domain decomposition technique for all datasets. The passing of the truck rendered difficult to identify the first bridge frequency. Conversely, the vehicle tests improved the identification of higher vibration modes. This is because the truck preferentially excites the bridge vertical response, which is associated with higher modes of vibrations, especially when a sudden stop of the vehicle occurs. Thus, carefully conducted vehicle-crossing tests provide detailed information about the bridge structure dynamics in the vertical direction. However, to identify lower modes, no vehicle on the bridge is preferred.

ARTICLE INFO

Article history:
Received 6 February 2017
Revised 12 March 2017
Accepted 17 March 2017

Keywords:
Box girder bridge
Modal identification
Frequency domain decomposition
Traffic loads

1. Introduction

Bridges in service are subject to a combination of various external loads, among which traffic loads are constantly imposed on the bridge structure. The dynamic response of a highway bridge is a complex phenomenon and it is less understood for curved bridges. During the past decades, various studies have attempted to study the dynamic response of curved bridges under moving truck loads. For instance, Billing (1984) presented the outcomes from a series of dynamic tests of 27 bridges in Ontario, Canada.

The datasets were obtained from more than 100 truck crossings for each bridge. It was pointed out bridge frequencies identified under a single truck load are typically larger than design estimations. A similar study was conducted in Switzerland (Cantieni, 1983). Later, Kim et al. (1996) presented the results from truck load tests conducted on seven bridges in the city of Detroit, Michigan. It was concluded truck loads on bridges are strongly site specific, even within the same geographic area. Senthilvasan et al. (2002) conducted a truck load test on the Turbot Street Bridge, a curved bridge in Australia, using a five-axle truck. It was found the deflections and strains (due to bending moments), are not amplified by the same amount. An important observation they made is the dynamic response not always increases with the speed of the vehicle, but it depends on the ratio of the vibration period to the traverse time. Brady et al. (2006) discussed the results from a truck load test on a simply supported bridge in Slovenia. More recently, Huang (2008) studied the deflection of a curved bridge under moving truck loads.

This paper aims to contribute the body of literature for the study of bridge response under traffic loads. The paper presents the findings of a series of vehicle-crossing tests conducted on the Fairview Road On-Ramp (FRO) bridge, located in Southern California, USA. The effect of truck speed and a sudden stop on the modal identification of the bridge structure is investigated.

* *Corresponding author*. Tel.: +90-462-3772628 ; Fax: +90-462-3772606 ; E-mail address: akkose@ktu.edu.tr (M. Akköse)
ISSN: 2149-8024 / DOI: https://doi.org/10.20528/cjsmec.2017.03.009

2. Frequency Domain Decomposition (FDD) Technique

The main problem associated with forced vibration tests on bridges, buildings, or dams stems from the difficulty in exciting the most significant modes of vibration in a low range of frequencies with sufficient energy and in a controlled manner. Fortunately, recent technological developments in transducers and analog-to-digital (A/D) converters have made it possible to accurately measure the very low levels of dynamic response induced by ambient excitations like wind or traffic. This has stimulated the development of output-only modal identification methods. Therefore, the performance of output-only modal identification tests became an alternative of great importance in the field of civil engineering. This allows accurate identification of modal properties of large structures at the commissioning stage or during their lifetime without interruption of normal traffic. Ambient excitation usually provides multiple inputs and a wide-band frequency content thus stimulating a significant number of vibration modes. For simplicity, output-only modal identification methods assume that the excitation input is a zero-mean Gaussian white noise. This means that real excitation can be expressed as the output of a suitable filter excited with white noise input. Some additional computational poles without physical meaning appear as a result of the white noise assumption (Cunha and Caetano, 2006).

Output-only modal identification of a civil infrastructure system is associated with the identification of its modal parameters. In the analysis the loads subjected to the system are unknown and the modal identification has to be carried out based on the responses only. Classically, forced vibration is applied to the structures where the applied excitation (input) can be measurable. However, it is often to face the case where the input excitation cannot be measured, i.e. ambient/traffic induced vibration. In such cases it is impractical, if not impossible to measure the excitation forces. Hence, the system identification techniques applied for the identification of modal parameters are separated in two main groups known as output-only and input-output techniques (Brincker et al., 2000).

The Frequency Domain Decomposition (FDD) was first introduced by Brincker et al. (2000). The FDD technique takes the singular value decomposition (SVD) of the spectral matrix which is decomposed into a set of auto spectral density functions, each corresponding to a single degree of freedom (SDOF) system. The results of the FDD are exact when the input excitation is white noise, the structure is lightly damped and when the mode shapes of close modes are geometrically orthogonal. If these assumptions are not satisfied the decomposition into SDOF systems is approximate, but still the results are significantly accurate.

2.1. Theoretical basis of the FDD technique

The relationship between the unknown inputs $x(t)$ and the measured responses $y(t)$ can be expressed as

$$G_{yy}(\omega) = \bar{H}(\omega) G_{xx} H(\omega)^T , \quad (1)$$

where G_{xx} is the *(rxr)* Power Spectral Density (PSD) matrix of the input, r is the number of inputs, $G_{yy}(\omega)$ is the *(mxm)* PSD matrix of the responses, m is the number of responses, $H(\omega)$ is the *(mxr)* Frequency Response Function (FRF) matrix and "¯" and T denote complex conjugate and transpose, respectively. The FRF can be written in partial fraction, i.e. pole/residue form

$$H(\omega) = \sum_{k=1}^{n} \frac{R_k}{\omega - \lambda_k} + \frac{\bar{R}_k}{\omega - \bar{\lambda}_k} , \quad (2)$$

where n is the number of modes, λ_k is the pole and R_k is the residue given by

$$R_k = \phi_k \gamma_k^T , \quad (3)$$

where ϕ_k and γ_k are the mode shape and the modal participation vectors, respectively. Usually, during experimental modal analysis using ambient/traffic vibration the inputs are unknown. Suppose the input is white noise, i.e. a random signals containing equal power within a fixed bandwidth at any center frequency, its PSD is a constant matrix, i.e. can be written as $G_{xx} = C$, then Eq. (1) becomes

$$G_{yy}(\omega) = \sum_{k=1}^{n} \sum_{s=1}^{n} \left[\frac{R_k}{\omega - \lambda_k} + \frac{\bar{R}_k}{\omega - \bar{\lambda}_k} \right] C \left[\frac{R_s}{\omega - \lambda_s} + \frac{\bar{R}_s}{\omega - \bar{\lambda}_s} \right]^H , \quad (4)$$

where superscript H denotes a complex conjugate and transpose. Multiplying the two partial fraction factors and making use of the Heaviside partial fraction theorem, after some mathematical manipulations, the output PSD can be reduced to a pole/residue form as follows

$$G_{yy}(\omega) = \sum_{k=1}^{n} \frac{A_k}{\omega - \lambda_k} + \frac{\bar{A}_k}{\omega - \bar{\lambda}_k} + \frac{B_k}{-\omega - \lambda_k} + \frac{\bar{B}_k}{-\omega - \bar{\lambda}_k} , \quad (5)$$

where A_k is the kth residue matrix of the output PSD. As for the output PSD itself the residue matrix is an *(mxm)* hermitian matrix and is given by

$$A_k = R_k C \left(\sum_{s=1}^{n} \frac{\bar{R}_s^T}{-\lambda_k - \bar{\lambda}_s} + \frac{R_s^T}{-\lambda_k - \lambda_s} \right) . \quad (6)$$

The contribution to the residue from the kth mode is given by

$$A_k = \frac{R_k C \bar{R}_s^T}{2\alpha_k} , \quad (7)$$

where α_k is minus the real part of the pole $\lambda_k = -\alpha_k + j\omega_k$. As it appears this term becomes dominating when the damping is light, and, thus, is the case of light damping, the residue becomes proportional to the mode shape vector

$$A_k \infty R_k C \bar{R}_k^T = \phi_k \gamma_k^T C \gamma_k \phi_k^T = d_k \phi_k \phi_k^T , \quad (8)$$

where d_k is a scalar constant. At a certain frequency ω only a limited number of modes will contribute significantly,

typically one or two modes. Let this set of modes be denoted by $Sub(\omega)$. Thus, in the case of a lightly damped structure, the response spectral density can always be written

$$G_{yy}(\omega) = \sum_{k\in Sub(\omega)} \frac{d_k \phi_k \phi_k^T}{\omega-\lambda_k} + \frac{\bar{d}_k \bar{\phi}_k \bar{\phi}_k^T}{\omega-\bar{\lambda}_k}. \quad (9)$$

This is a modal decomposition of the spectral matrix. The expression is similar to the results one would get directly from Eq. (1) under the assumption of independent white noise input, i.e. a diagonal spectral input matrix.

2.2. FDD identification algorithm

In the FDD identification, the first step is to estimate the PSD matrix. The estimate of the output PSD $\hat{G}_{yy}(\omega)$ known at discrete frequencies $\omega = \omega_i$ is then decomposed by taking the Singular Value Decomposition (SVD) of the matrix

$$\hat{G}_{yy}(\omega) = U_i S_i U_i^H , \quad (10)$$

where the matrix $U_i = [u_{i1}, u_{i2}, \dots, u_{im}]$ is a unitary matrix holding the singular vectors u_{ij}, and S_i is a diagonal matrix holding the scalar singular values s_{ij}. Near a peak corresponding to the kth mode in the spectrum this mode, or maybe a possible close mode, will be dominating. If only the kth mode is dominating there will only be one term in Eq. (9). Thus, in this case, the first singular vector u_{i1} is an estimate of the mode shape

$$\hat{\phi} = u_{i1} , \quad (11)$$

and the corresponding singular value is the auto power spectral density function of the corresponding single degree of freedom system, refer to Eq. (9). This PSD function is identified around the peak by comparing the mode shape estimate $\hat{\phi}$ with the singular vectors for the frequency lines around the peak. As long as a singular vector is found that has a high modal assurance criterion (MAC) value with $\hat{\phi}$, the corresponding singular value belongs to the SDOF density function.

From the piece of the single degree of freedom (SDOF) density function obtained around the peak of the PSD, the natural frequency and the damping can be obtained. The piece of the SDOF PSD was taken back to the time domain by an Inverse Fast Fourier transform (IFFT), and the frequency and the damping was simply estimated from the crossing times and the logarithmic decrement of the corresponding SDOF autocorrelation function.

In the case where two modes are dominating, the first singular vector will always be a good estimate of the mode shape of the strongest mode. However, in the case where the two modes are orthogonal, the first two singular vectors are unbiased estimates of the corresponding mode shape vectors.

In the case where the two modes are not orthogonal, the bias on the mode shape estimate of the dominant mode will typically be small, but the bias on the mode shape estimate of the weak mode will be strong. Thus, one has to estimate the mode shapes for the two close modes at two different frequency lines, one line where the first mode is dominant and another frequency line where the second mode is dominant.

3. Description of Bridge, Monitoring System and Vehicle Crossing Tests

3.1. Description of the Fairview Road On-Ramp (FRO) Bridge

The Fairview Road On-Ramp Overcrossing (FRO) Bridge (Figs. 1, 2) is located in the city of Costa Mesa on the Interstate 405, one of the busiest routes in Southern California. The FRO Bridge is a four-span and one-lane continuous concrete box girder bridge. In plan the bridge is slightly curved with double curvature and radius of curvature of 600m (1,968.5ft). Summary plan and section details are shown in Fig. 3. The length of the bridge is 224m (735ft) along the "F2" line, in which the lengths of spans running from south to north are 52.5, 59.5, 59.5 and 52.5m (172.2, 195.2, 195.2 and 172.2ft), respectively. The super-structure consists of a three-cell cast-in-place pre-stressed and post-tensioned box girder which is aligned 6% to the horizontal. The deck is supported on two monolithic columns and sliding bearings at opposite abutments. Concrete traffic barriers are approximately 0.8m (1.75ft) high, attached to the outer edges of the road.

The sub-structure consists of three single column bents and two tall-seat type abutments. The main bent reinforcement is anchored in solid concrete diaphragms filling the girder void at bent locations, providing continuity between column and box girder. The columns have circular cross-sections with 2.14m (7ft) as the diameter. The bents are founded on square RC pad footings and the abutments are supported on rectangular footings.

Fig. 1. A view of the Fairview Road On-Ramp Overcrossing (FRO) Bridge.

Fig. 2. A close look of the Fairview Road On-Ramp Overcrossing (FRO) Bridge.

3.2. FRO Bridge monitoring system

The FRO Bridge is instrumented with a total of 21 accelerometers (Fig. 4). The accelerometers are either uni-, bi- or tri-axial force-balance servo-type accelerometers. An easy access to the data recorder is possible since it is installed on the ground below the deck at the beginning of the bridge. More details on the instrumentation can be found in Gomez (2011).

3.3. Description of vehicle crossing tests on FRO Bridge

A water truck with capacity of 2,000 gal, was used in the vehicle crossing tests (Fig. 5). At full capacity the truck has a gross vehicle weight of 138 kN. This weight was distributed as 49 kN at the front axle and 89 kN at the rear axle. The distance from the front axle to the rear axle is 3.96m. Although this truck is not one of the heaviest vehicles that could potentially pass on the FRO Bridge, it has a considerable mass to induce an adequate bridge response.

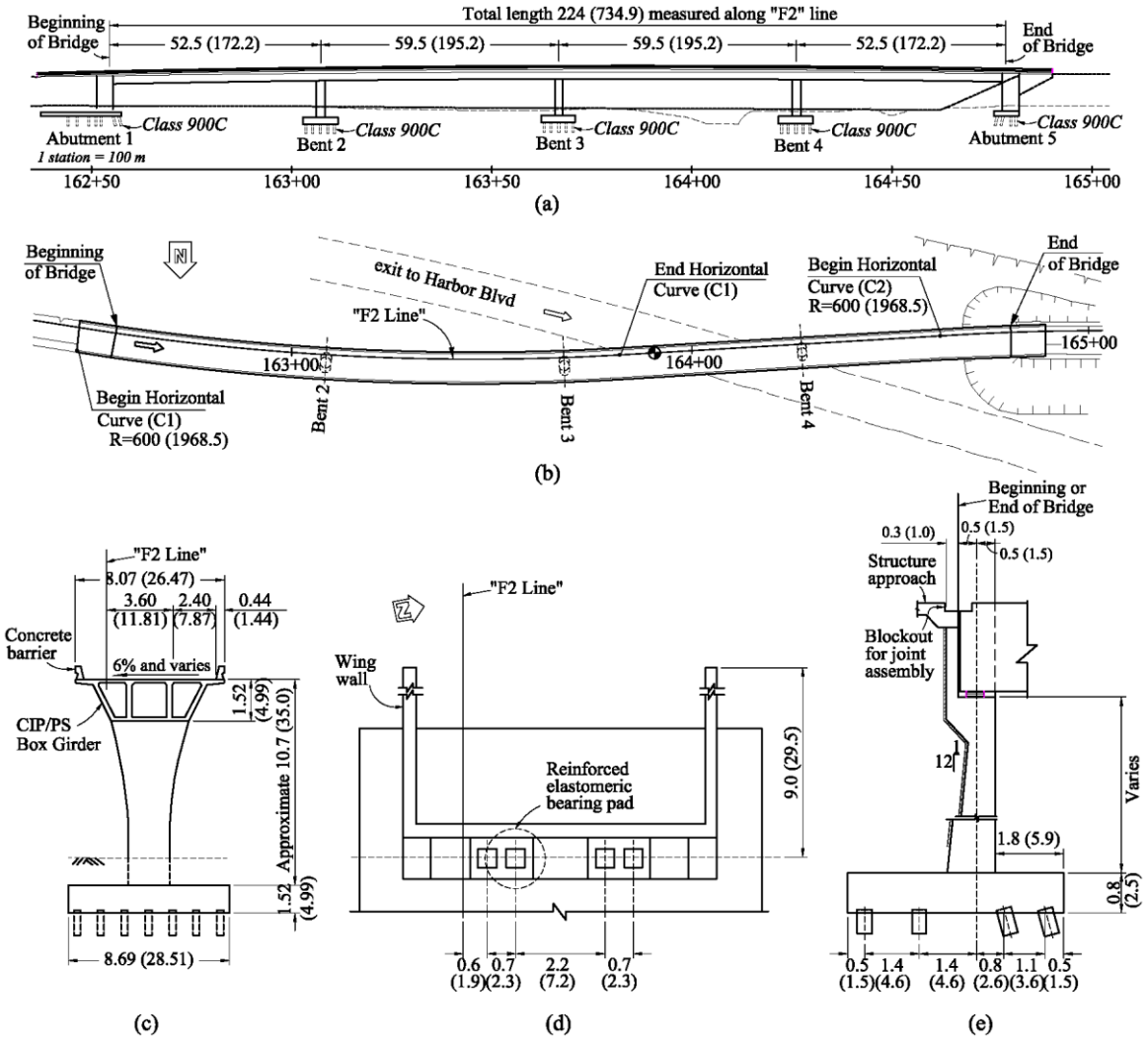

Fig. 3. Structural details of the Fairview Road On-Ramp Overcrossing (FRO) Bridge: (a) elevation; (b) plan view; (c) bent typical section; (d) abutment layout plan view; (e) typical abutment section (dimensions in m (ft)).

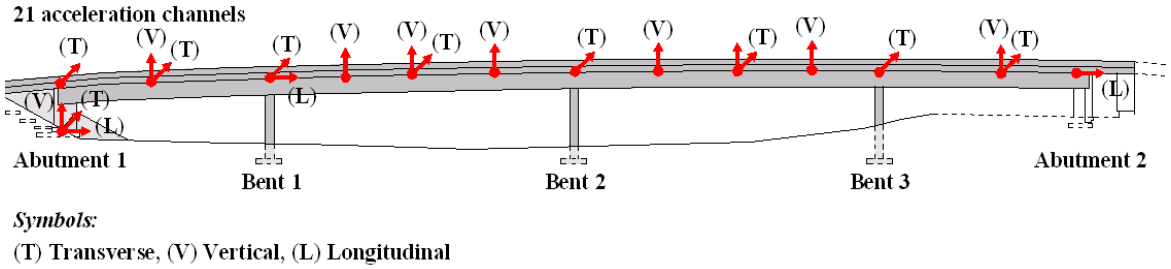

Fig. 4. Sensor layout at FRO Bridge.

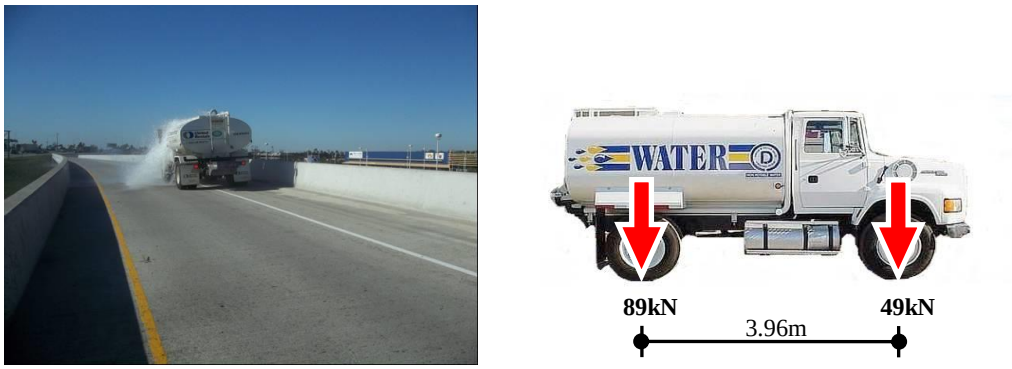

Fig. 5. Truck weight and dimensions.

During the vehicle-crossing tests (Fig. 6), after the bridge is closed to public traffic, the truck entered the beginning of the bridge (Abutment 1) with a constant speed of 8 km/h (5 mph) and made a complete stop at the middle of the second span. After one minute, the truck started moving again at a speed of approximately 8 km/h until it arrived at the middle of the third span where it made a second complete stop. After one minute, the truck resumed the trip and left the bridge at a speed of approximately 8 km/h. Afterwards, the truck made a U-turn and entered from the end of the bridge (Abutment 5) and made two stops, one minute each, at the same locations as going forward (see Fig. 6). Then, the test vehicle exits the bridge at speed of 8 km/h and completes its first round trip.

Another test consisted in driving the test vehicle at a speed of approximately 72-81 km/h (45-50 mph). When the vehicle arrived at the middle of the second span, the breaks were suddenly applied to generate an impact load on the bridge. Then, the truck proceeded at 8 km/h and left the bridge. Next, the truck made a U-turn for the final trip. In the last trip, the truck entered at the end of bridge and accelerated to reach a speed of approximately 48-56 km/h (30-35 mph). Another sudden break was applied at the middle of the third span. The test vehicle resumed the trip at 8 km/h and left the bridge.

4. Results and Discussion

Fig. 7 shows the acceleration time-history response at sensor locations during the vehicle-crossing tests. It was found 7 accelerometers (#'s 9, 14, 17-21) were malfunctioning at the time of the tests. Since the accelerometers were installed inside the box girder, it was not possible to access for a detailed inspection of the sensors and the reasons for the malfunctioning were unknown. Therefore, the remaining 14 accelerometers were used to study the bridge response. Despite the malfunctioning sensors, it was still possible to attain an accurate identification of the modal parameters of the bridge. The remaining sensors provided the adequate information in order to identify the modes of vibration with high confidence.

In Fig. 7, the bridge response acceleration time-histories were subdivided into nine groups, identified by colors, according to the level of acceleration. It can be observed the magnitude of the vertical response of the bridge was drastically increased (about 200%) for the tests where a sudden stop of the test vehicle was applied. Afterwards, each group of accelerations was analyzed to identify the bridge modal parameters.

4.1. Bridge modal identification

The frequency domain decomposition (FDD) was applied to the acceleration datasets to identify bridge modal parameters. The FDD technique was introduced by Brincker et al. (2000) as an alternative to other frequency domain system identification techniques. The FDD technique has been widely used for system identification of bridges in recent years (Kim et al., 2003; Feng et al., 2004; Chen et al., 2006; Gomez et al., 2011; Gomez, 2011).

The power spectral density functions used by the FDD were estimated using Hanning windows with 60% overlap. In order to reduce background noise, a butter-worth infinite impulse response filter of order 8 was applied to

the data with a pass-band defined by a lower frequency of 1 Hz and a higher frequency of 10 Hz. The FDD results are shown in Fig. 8. The identification of the natural frequencies is presented for the nine groups of bridge responses separately. The natural frequencies are identified at approximately 1.465, 2.002, 2.295, 2.881, and 3.076 Hz. It can be seen that natural frequencies are consistent for each set of data.

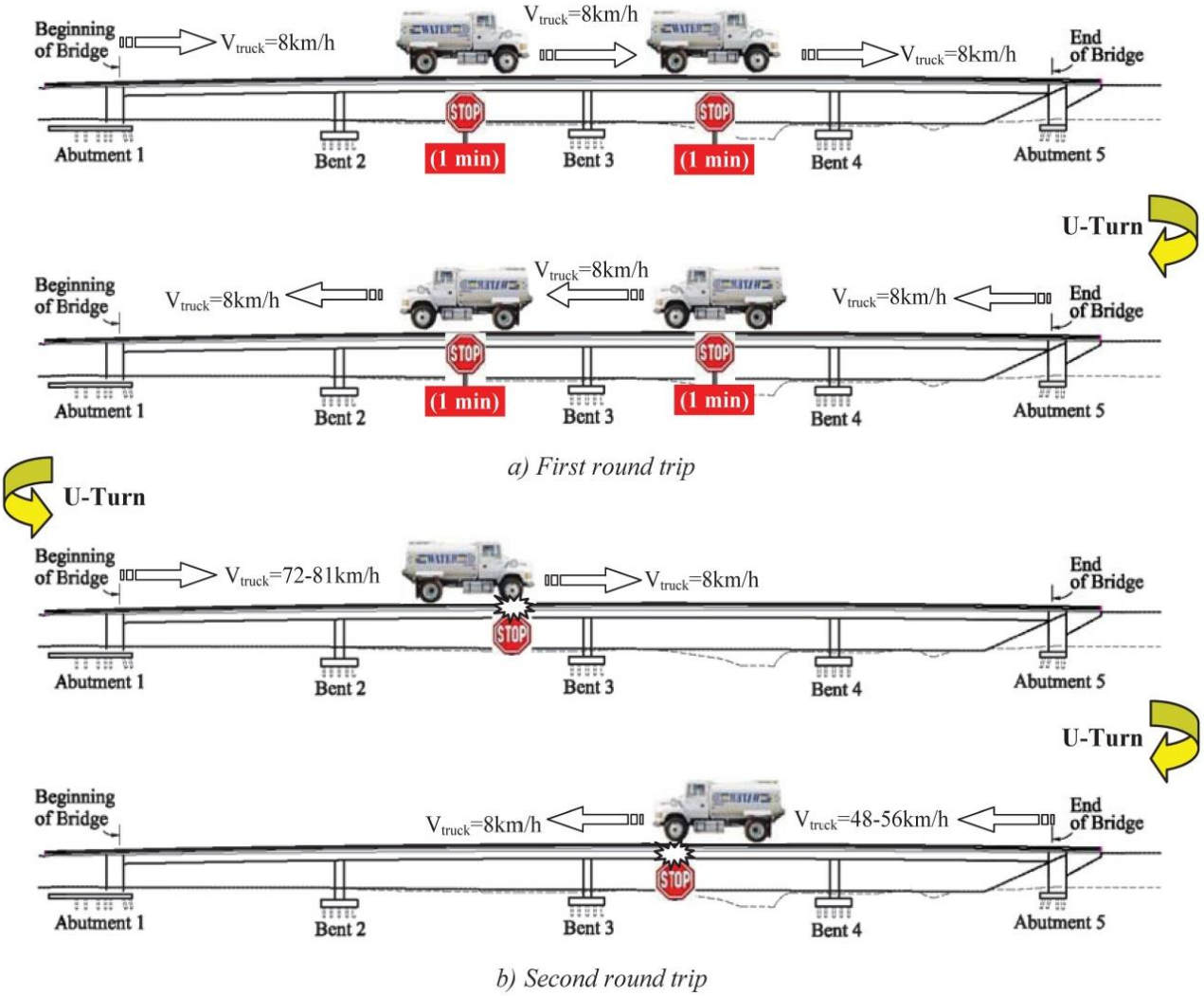

Fig. 6. Description of vehicle crossing tests (total test duration was approximately 18 minutes).

In addition to bridge natural frequencies, partial mode shapes (as the bridge is instrumented at discrete locations only) are plotted for the first three modes (see Fig. 9). Although the first three modes exhibit some combination of vertical and horizontal motions, it is clear that the first mode (f_1 = 1.465 Hz) is a lateral rocking mode about the longitudinal axis of the bridge with the three bents in phase. This mode is clearly identified from the time history segment from 610 s to 800 s (cyan color in Fig. 7). During this time segment no vehicle was on the bridge. It is noted this mode is not always identified (or it has a low peak amplitude in the frequency plots) because in most of the data sets the data contain the response of the bridge due to the truck load, which predominantly excites the vertical modes. This is clearly observed in the next two modes of vibration (f_2 = 2.002 Hz and f_3 = 2.295 Hz), which are a combination of vertical bending and torsion of the bridge deck.

From the results presented above, it can be sensibly argued the passing of the truck rendered difficult to identify the first bridge frequency. Conversely, the vehicle tests improved the identification of higher vibration modes. This is because the truck tends to excite the bridge vertical response, which is associated with higher modes of vibration, especially when a sudden stop of the vehicle occurs (magenta and blue last two segments, from 800 s to 1098 s in Fig. 7).

Another observation from the identification results is the natural frequencies are practically the same for different speeds of the truck as different segments in the time histories were recorded for different speeds as described earlier. Therefore, the modes of vibration were not influenced by truck speeds, which ranged from 8 to 80 km/h. Further studies are recommended to study the effect of truck speed on the modal identification by using higher vehicle velocities.

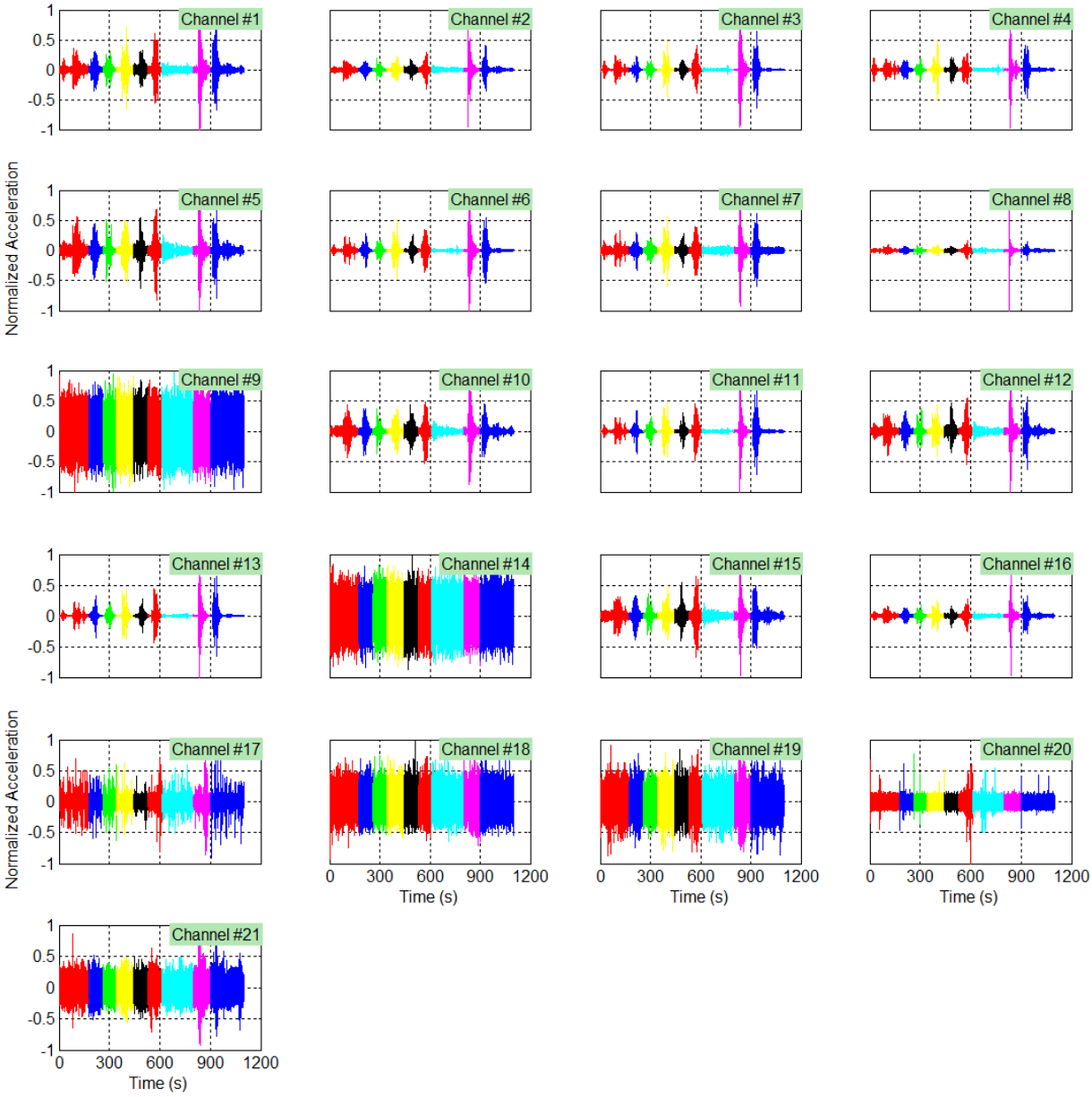

Fig. 7. Normalized acceleration time-history response at sensors during the vehicle tests.

5. Conclusions

In this study, the findings of a series of vehicle crossing test on a concrete bridge are presented. Acceleration response datasets were recorded during the tests. The natural frequencies of the bridge were determined using the frequency domain decomposition (FDD) technique for all datasets. The identification results show that the first frequency is associated with lateral mobilization of the deck and bending of the columns whereas higher modes are associated with the vertical and torsional mobilization of the deck.

It was observed that the passing of the truck renders difficult to identify the first bridge frequency. This is because the first bridge frequency is associated with bending of the columns and lateral mobilization of the deck. Conversely, the vehicle tests improved the identification of higher vibration modes because these are associated with vertical bridge response. This is more apparent for the crossing vehicle tests where a sudden stop was applied inducing a bigger vertical force on the bridge. In this case, the magnitude of the vertical response of the bridge is drastically increased (about 200%).

Since no change in the identification results was observed due to an increase in truck speed, it is concluded the amplification of the magnitude of the bridge response due to an increased vertical load (heavier vehicles or a sudden stop), exceeds any velocity effect.

It is the authors' opinion that carefully conducted vehicle-crossing tests provide detailed information about the bridge structure dynamics in the vertical direction. However, to identify lower modes, no vehicle on the bridge is preferred. Moreover, much higher truck velocities than those attained in this study (a maximum of approximately 80 km/h) are recommended in order to study any effects on bridge response.

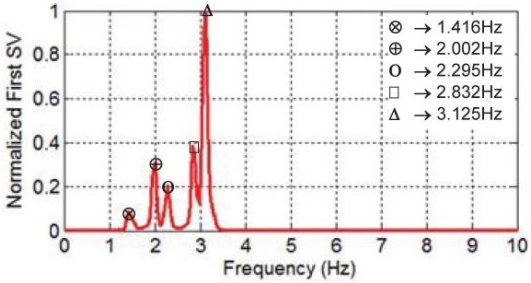

For 1st group data (first red color section in Fig. 6)

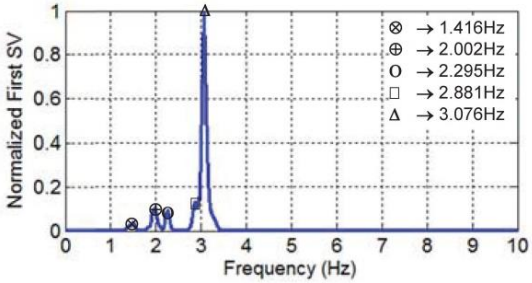

For 2nd group data (first blue color section in Fig. 6)

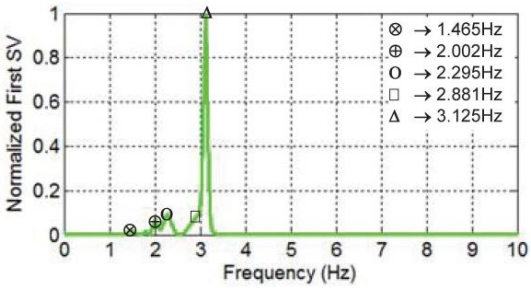

For 3rd group data (green color section in Fig. 6)

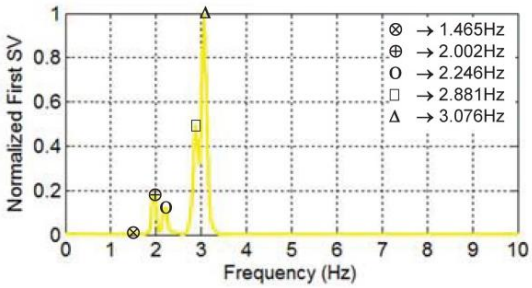

For 4th group data (yellow color section in Fig. 6)

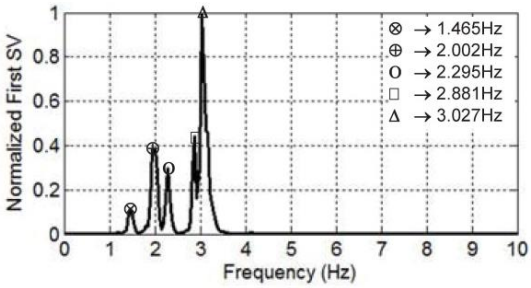

For 5th group data (black color section in Fig. 6)

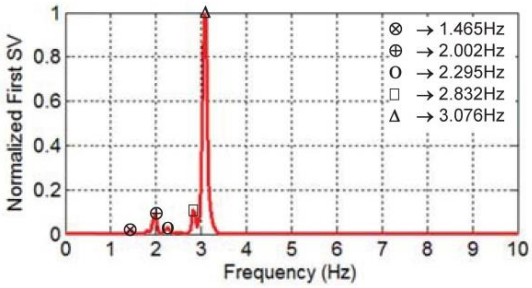

For 6th group data (second red color section in Fig 6)

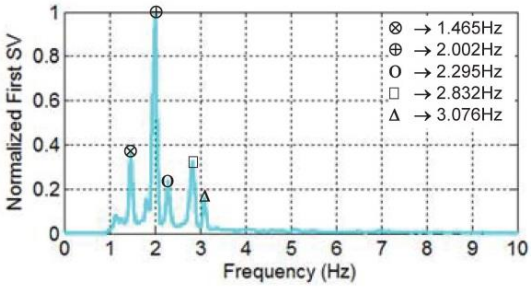

For 7th group data (cyan color section in Fig. 6)

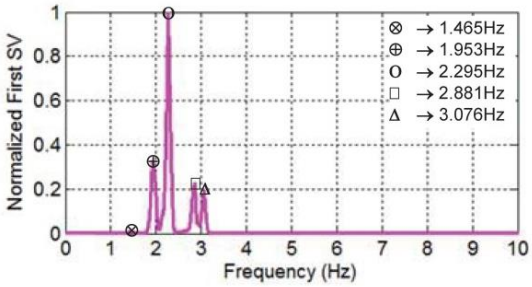

For 8th group data (magenta color section in Fig. 6)

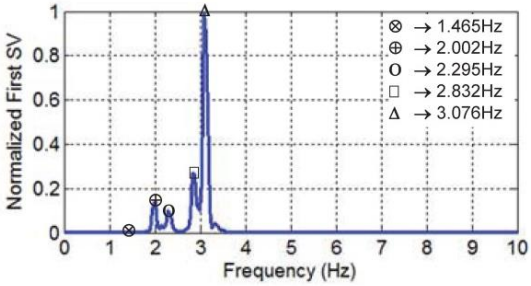

For 9th group data (second blue color section in Fig. 6)

Fig. 8. Normalized first SV obtained from FDD applied to data recorded during vehicle crossing tests.

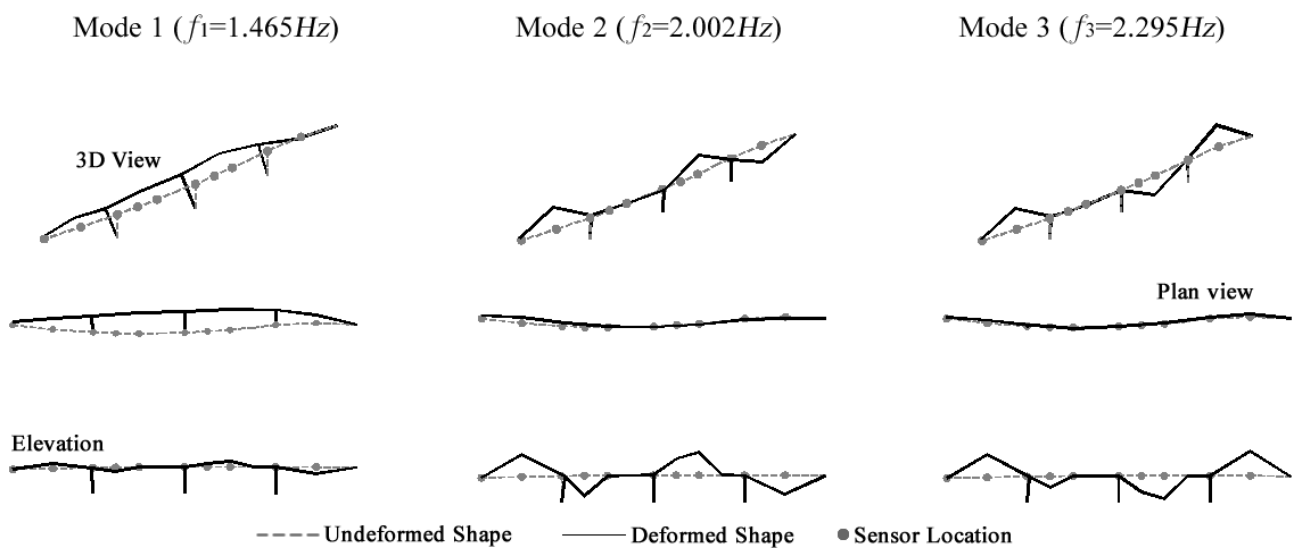

Fig. 9. Identified partial mode shapes of the FRO Bridge.

Acknowledgements

This research was supported by the Scientific and Technical Research Council of Turkey (TUBITAK) under the 2219-Foreign Postdoctoral Research Scholarship Program. The authors also wish to thank the support of the California Department of Transportation.

REFERENCES

Billing JR (1984). Dynamic loading and testing of bridges in Ontario. *Canadian Journal of Civil Engineering*, 11(4), 833-843.

Brady SP, O'Brien EJ, Žnidarič A (2006). Effect of vehicle velocity on the dynamic amplification of a vehicle crossing a simply supported bridge. *Journal of Bridge Engineering*, 11(2), 241-249.

Brincker R, Zhang L, Andersen P (2000). Modal identification from ambient response using frequency domain decomposition. *Proceedings of the 18th International Modal Analysis Conference (IMAC18), Society for Experimental Mechanics*, San Antonio, TX, USA, 625-630.

Cantieni R (1983). Dynamic load tests on highway bridges in Switzerland. Rep. No. 211, *Eidgenossische Material-prufungs-und Versuchsantalt (EMPA)*, Dubendorf, Switzerland.

Chen Y, Feng MQ, Tan CA (2006). Modeling of traffic excitation for system identification of bridge structures, *Computer-Aided Civil and Infrastructure Engineering*, 21(1), 57-66.

Feng MQ, Kim DK, Yi J-H, Chen Y (2004). Baseline models for bridge performance monitoring, *Journal of Engineering Mechanics*, 130(5), 562-569.

Gomez HC (2011). System identification of highway bridges using long-term vibration monitoring data, *Ph.D. thesis*, University of California, Irvine, USA.

Gomez HC, Fanning PJ, Feng MQ, Lee S (2011). Testing and long-term monitoring of a curved concrete box girder bridge, *Engineering Structures*, 33(10), 2861-2869.

Huang D (2008). Dynamic loading of curved steel box girder bridges due to moving vehicles. *Structural Engineering International*, 18(4), 365-372.

Kim CY, Jung DS, Kim NS, Kwon DS, Feng MQ (2003). Effect of vehicle weight on natural frequencies of bridges measured from traffic-induced vibration. *Earthquake Engineering and Engineering Vibration*, 2(1), 109-115.

Kim S, Sokolik A, Nowak A (1996). Measurement of truck load on bridges in Detroit, Michigan, area. Transportation Research Record: *Journal of the Transportation Research Board*, 1541(1), 58-63.

Senthilvasan J, Thambiratnam DP, Brameld GH (2002). Dynamic response of a curved bridge under moving truck load. *Engineering Structures*, 24(10), 1283-1293.

Challenge Journal of Structural Mechanics

Modelling of non-linear seismic ground response using elasto-plastic constitutive framework within a finite element soil column model

Azeddine Chehat [a], Zamila Harichane [b,*], Amina Sadouki [b]

[a] *Department of Civil Engineering, University Djilali Bounaama, 44000 Khemis Meliana, Algeria*
[b] *Geomaterials Laboratory, University Hassiba Benbouali of Chlef, 02000 Chlef, Algeria*

ABSTRACT

The prediction of seismic ground response is conditioned by the knowledge of each material behavior of soil deposits. The recourse to plasticity criterion to simulate cyclic behavior of soils under seismic loading is becoming more realistic. In this study, an elasto-plastic constitutive equation is cast within the framework of one dimensional finite element (FE) soil column model to account for the spatial and material nonlinearity of the secant shear modulus. To account of the spatial non linearity, shear modulus is written in terms of rigid base shear modulus and height of the soil column, while for material nonlinearity, the shear modulus degradation is deducted by the application of the isotropic evolution of the Von Misès criterion. Obtained results proved the efficiency of the proposed methodology and the predictive capability of the elaborated elastoplastic model which captures both small- and large-strain behaviors. They likewise highlight the important roles that play the spatial and material shear modulus variation in the prediction of the seismic soil responses.

ARTICLE INFO

Article history:
Received 26 January 2017
Revised 25 April 2017
Accepted 13 May 2017

Keywords:
Von Misès criterion
Cyclic behaviour
Shear modulus
Seismic response
Bessel's function
Large-strain

1. Introduction

Under seismic loadings, soil behavior is highly nonlinear. For this kind of loading, the soil behaves strongly non-linear due to the degradation of the shear modulus (Mercado et al., 2015). So, adequate constitutive equation should be used to accurately predict the nonlinear soil behavior. For several decades, the soil behavior under different loading conditions was satisfactorily studied by numerical methods, particularly by the finite element method (FEM). The one-dimensional (1-D) modelling of soil profiles by the FEM under cyclic loading was widely used by several researchers (Hashash and Park, 2002; Stewart et al., 2008; Vasileios et al., 2012; Kaklamanos et al., 2015; Mercado et al. 2015)

The prediction of the nonlinear response depends on several factors such as geotechnical data, especially the variation of shear modulus, and the mathematical model chosen to describe the stress-strain relationship (τ-γ). Harichane et al. (2011a) used a 1-D Finite Elements (FE) model to describe the nonlinear behavior of geomaterials under seismic loads. The 1-D FE model was validated by Harichane et al. (2011b) using seismic data recorded during the 2003 Boumerdes earthquake (M=6.9), deeply studied by Khellafi et al. (2013), and soil profile's characteristics identified by an inverse analysis carried by Harichane et al. (2012).

The nonlinear soil responses may be mainly predicted in terms of accelerations, velocities, displacements, strain, and stresses. This response can be obtained at any depth of a soil profile by considering spatial and material variation of shear modulus. The last one is commonly represented in puissance description (Abdelghaffar and Koh, 1981). However, there is not a universal constitutive equation to describe the behavior of the soils under any kind of excitations but some ones exist in literature for specified materials.

The present study is mainly intended to carry out an efficient methodology to predict the nonlinear cyclic response of a soil profile using the FEM together with the Von Misès elasto-plastic criterion. A simple case study concerned with the behavior a soil profile excited at its

* *Corresponding author*. Tel.: +213-027-776398 ; Fax: +213-027-721794 ; E-mail address: zharichane@gmail.com (Z. Harichane)
ISSN: 2149-8024 / DOI: https://doi.org/10.20528/cjsmec.2017.05.011

rigid base by a first order Ricker signal is carried out. The spatial variation of the shear modulus is captured by an exponential expression depending on the height and the shear modulus at the base of the soil profile. A 1-D FE model is translated in a computer program, in the MATLAB environment, incorporating the Von-Misès criteria with a linear hardening in both small- and large-strain analyses. The dynamic governing equation is solved by Newmark's non-linear integration with modified Newton's iteration, detailed in (Bathe, 1996).

Results are obtained in terms of depth-dependent distribution of maximum displacement, depth-dependent distribution of maximum acceleration with respect to that at the base of the soil profile, and stress-strain hysteretic loop, where the effect of spatial and material non-linearity of shear modulus as well as small- and large-strain assumptions are examined.

2. Basic Equations

The forces acting on a soil element with dimensions (dx, dy, dz) in a soil profile (Fig. 1) are: *(i)* the inertia force (F_I), *(ii)* the shearing force (S_{xy}), and *(iii)* the earthquake force (F_g), given, respectively, by Eqs. (1) to (3).

$$F_I = \rho dxdydz.\ddot{u}(x,y,t)\,, \tag{1}$$

$$S_{xy} = dxdz.\frac{\partial \tau_{xy}(y,t)}{\partial y}\,, \tag{2}$$

$$F_g = \rho dxdydz.\ddot{u}_g(t)\,, \tag{3}$$

where ρ is the mass density of the soil element, $\partial\tau_{xy}(y,t)/\partial y$ the variation of the shear stress in the soil element due to a base shear motion $\ddot{u}_g(t)$, and $\ddot{u}(x,y,t)$ the soil element acceleration. The equations of motion of the soil element is then;

$$\rho.\ddot{u}(x,y,t) = \frac{\partial \tau_{xy}(y,t)}{\partial y} - \rho\ddot{u}_g(t)\,. \tag{4}$$

The original displacement is represented by nodal displacements and the stresses are interpreted by the associated nodal forces. The governing equation of motion is described for the j^{th} step as (Elgamal, 1991; Gu et al., 2009; Hashash and Park, 2001).

$$[M]\{\Delta\ddot{u}\}_j + [C]_j\{\Delta\dot{u}\}_j + \int_\Omega [B]_j^T\{\Delta\sigma\}_j d\Omega = -[M]\{\Delta\ddot{u}_g\}\,. \tag{5}$$

In Eq. (5), $[\mathrm{B}]_j^T$ defines the displacement-strain matrix. [M] and $[\mathrm{C}]_j$ denote the mass and damping matrices, respectively. The damping matrix $[\mathrm{C}]_j$ is proportional to the mass and the stiffness matrices.

$$[C]_j = \alpha_1[M] + \alpha_2[K]_j\,, \tag{6}$$

where α_1 and α_2 are coefficient to be determined (Harichane et al., 2011b; Chopra, 2012).

The time domain step-by-step solution of the semi-discrete matrix equation (5) is performed using the Newmark family methods (Bathe, 1996). From Eq. (5), the material or kinematic nonlinearity occurs in the internal forces $\int_\Omega [\mathrm{B}]_j^T\{\Delta\sigma\}_j d\Omega$ that depends on the elasto-plastic stress $\{\Delta\sigma\}_j$ (Dunne and Petrinic, 2006).

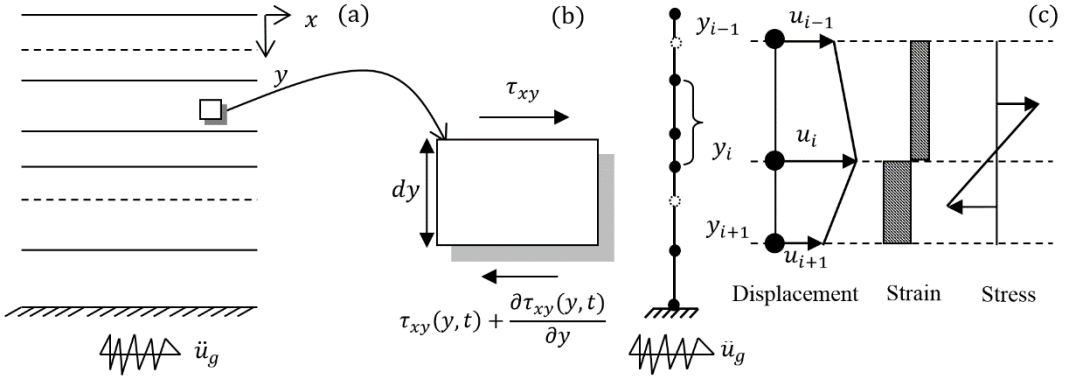

Fig. 1. Schematization of: (a) soil profile; (b) stress acting on a soil finite element; and (c) discrete model with details illustrating the definition of displacement, strain and stress.

3. Free Vibrations

An essential step in the determination of the damping matrix (Eq. (6)), is the calculation of the natural frequencies. In this way, the equation of motion in free vibration, also called wave equation, is solved using Bessel's functions as usually done in such problems. Citing, without exclusivity, the work of Pecker (1995) in which eigenfrequencies of a soil profile with shear wave velocity varying in power exponent (B) of depth were obtained using Bessel's function of order *(B-1)/(2-B)* and validated experimentally. Similarly, Afra and Pecker (2002) solved the wave equation for a soil deposit with shear modulus increasing with power exponent of depth to obtain the surface spectrum derived from an accelerogram compatible with the Eurocode 8 response spectrum.

In the present study, the linear elastic shear stress-strain response is expressed by

$$\tau_{xy}(y,t) = G(y)\frac{\partial u(x,y,t)}{\partial y}\,. \tag{7}$$

In Eq. (7), $\partial u(x,y,t)/\partial y$ is the shear strain and $G(y)$ the shear modulus of non-homogeneous soil profile assumed in the following form (Elgamal, 1991; Dakoulas and Gazetas, 1985).

$$G(y) = G_b(\frac{y}{h})^B \,, \tag{8}$$

where G_b is the shear modulus at the base of the soil profile, h its height and $0 \leq B \leq 1$.

A solution of the eigenvalue problem which corresponds to Eq. (5) may be obtained by setting

$$u(y,t) = \psi(y)e^{i\omega t} \,, \tag{9}$$

which yields to the following Bessel's equation.

$$y^2\frac{d^2\psi}{dy^2} + By\frac{d\psi}{dy} + \frac{\rho\omega^2 h^B}{G_b}y^{2-B}\psi = 0 \,, \tag{10}$$

The solution of Eq. (10) may be obtained in the form of,

$$\psi = (y)^{\frac{1-B}{2}}\left[C_1 J_{\frac{(1-B)}{(2-B)}}(\frac{2}{(2-B)}\sqrt{\frac{\rho_i\omega^2 h^B}{G_b}}y^{(\frac{2-B}{2})}) + C_2 J_{-\frac{(1-B)}{(2-B)}}(\frac{2}{(2-B)}\sqrt{\frac{\rho_i\omega^2 h^B}{G_b}}y^{(\frac{2-B}{2})})\right], \tag{11}$$

while C_1 and C_2 are integration constants.

For a soil profile of thickness h, for which the shear wave velocity V is equal to V_b, it can be shown that the eigen frequencies are given by

$$\omega_i = \frac{a_i(2-B)}{2}\frac{V_b}{h} \,, \tag{12}$$

where the a_i values are the roots of frequency equation $J_{-\frac{(1-B)}{(2-B)}}(a_i) = 0$ which depend on the inhomogeneity B (Dakoulas and Gazetas, 1985).

The plots of the first kind of Bessel's function $J_0(\omega_i/2\pi)$, $J_{0.25}(\omega_i/2\pi)$, $J_{1/3}(\omega_i/2\pi)$, $J_{0.4}(\omega_i/2\pi)$ and $J_{0.5}(\omega_i/2\pi)$ are shown in Fig. 2 for different materials $(0 \leq B \leq 1)$. After Afra and Pecker (2002), many soil deposits undergo variation of shear modulus in the form of Eq. (8) such that for cohesionless materials the value of B varies from 0.45 to 0.6 while for normally consolidated clays B varies from 0.8 to 1.

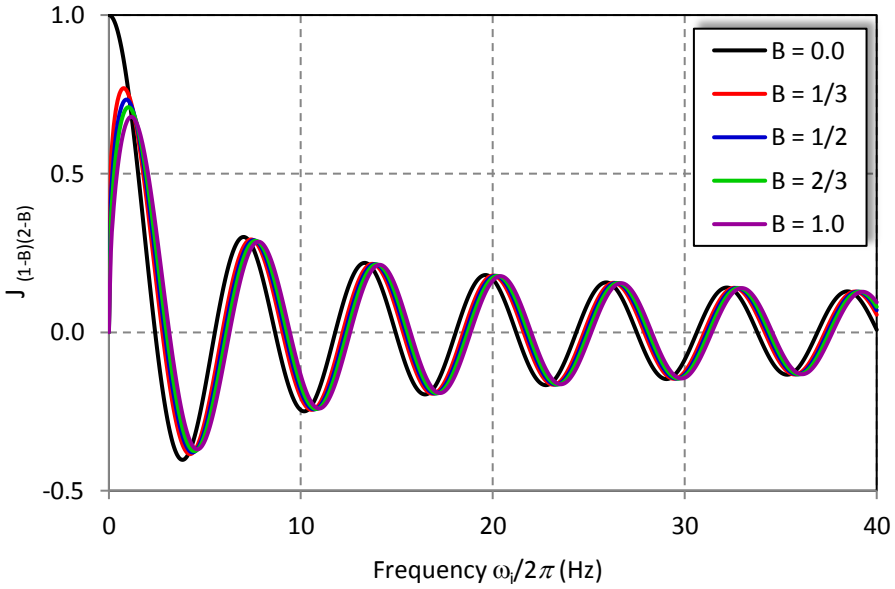

Fig. 2. Bessel' function of the first kind $J_{\frac{1-B}{2-B}}, B \in [0,1]$.

4. Integration of the Constitutive Equation for Material Nonlinearity

A one-dimensional elasto-plastic model based on the flow or incremental theory of plasticity according to Von-Misès criterion is used to describe the nonlinear hysteretic shear stress versus shear strain behavior of the soil material (Dunne and Petrinic, 2006). The constitutive equation is written in the following form.

$$f^{VM} = \sqrt{3J_2} - Y = 0 \,. \tag{13}$$

The parameter Y represents the size of the yield surface which defines the region of constant plastic shear modulus.The yield criterion determines the stress level at which plastic deformation begins and can be written in the general form (Fig. 3).

$$f(\tau, r) = 0 \,, \tag{14}$$

The consistency condition is written for an incremental change in stress and effective plastic strain $(f_{n+1}(\tau_{n+1}, \lambda_{n+1}) = 0)$ where $d\lambda$ is the plastic multiplier. This can be expanded as

$$f(\tau_{n+1}, \lambda_{n+1}) = f_n(\tau_n, \lambda_n) + \frac{\partial f_{n+1}}{\partial \tau_n}d\tau_n + \frac{\partial r_{n+1}}{\partial r_n}d\lambda_n = 0 \,, \tag{15}$$

with

$$\frac{\partial f_{n+1}}{\partial \tau_n}d\tau_n + \frac{\partial r_{n+1}}{\partial r_n}d\lambda_n = 0 \,. \tag{16}$$

Fig. 4 schematizes the essential steps for the determination of the elastoplastic stress by the trapezoidal rule integration.

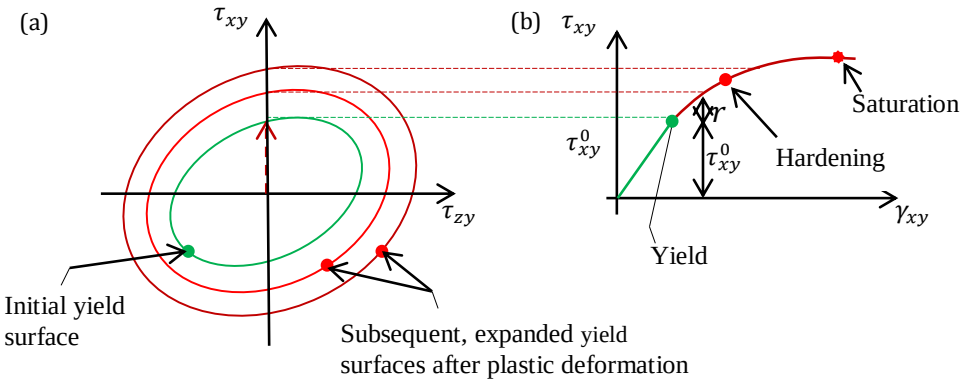

Fig. 3. (a) Isotropic hardening, in which the yield surface expands with plastic deformation; (b) the corresponding uniaxial stress-strain curve.

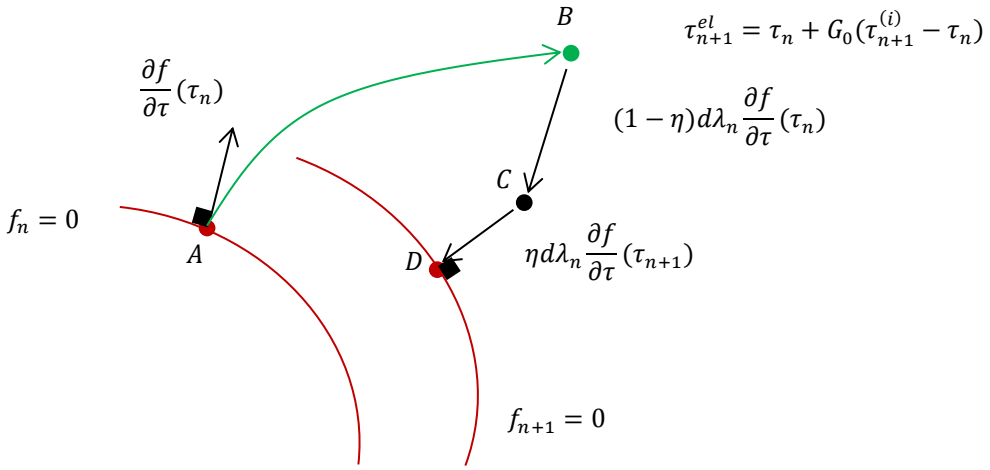

Fig. 4. Calculation of elastoplastic stress by a trapezoidal integration scheme.

According to Fig. 4, if $\eta = 0$ the diagram is the explicit Euler one, which generally requires a sub increment, and corrects at the end of the time. For $\eta = 0$, the implicit Euler method "Backward Euler" is placed. A first-order Taylor expansion about the point B in Fig. 4, *i.e.* (τ_{n+1}^{el}) gives

$$f_{n+1} = f_{n+1}^{el} + \frac{df_{n+1}^T}{d\tau_{n+1}^{el}} d\tau + \frac{df_{n+1}}{dr_{n+1}} dr = 0\,. \tag{17}$$

The total strain $d\varepsilon$ has already been applied in moving from point A to point B in Fig. 4, since $d\tau$ can be written as

$$d\tau = -d\lambda G_0 \left(\frac{df_{n+1}}{d\tau_{n+1}^{el}}\right). \tag{18}$$

Eq. (17) becomes

$$f_{n+1} = f_{n+1}^{el} - d\lambda \frac{df_{n+1}^T}{d\tau_{n+1}^{el}} G_0 \frac{df_{n+1}}{d\tau_{n+1}^{el}} - d\lambda H = 0\,. \tag{19}$$

The set of non-linear equations (17-19) is subsequently cast in a format of local residuals (in the sense that the residuals are defined at integration point level)

$$\begin{cases} r_\lambda = d\lambda - \left(\dfrac{f_{n+1}^{el}}{\frac{df_{n+1}^T}{d\tau_{n+1}^{el}} G_0 \frac{df_{n+1}}{d\tau_{n+1}^{el}} + H}\right) \\ r_\tau = \tau_{n+1} - \left(\tau_{n+1}^{el} - d\lambda G_0 \frac{df_{n+1}}{d\tau_{n+1}^{el}}\right) \end{cases}. \tag{20}$$

This system can be solved using an iterative procedure such *as Newton–Raphson* method (Bathe, 1996) to reduce r_λ and r_τ to (almost) zero while the final stresses should satisfy the yield criterion, $f_{n+1} = 0$. The term $-(1/d\lambda)(df/dr)dr$ is the hardening function H obtained to be the local slope of the uniaxial stress/plastic strain curve (Eq. (21)).

$$H = \frac{d\tau}{d\varepsilon^p} = \frac{G_T}{1 - \frac{G_T}{G_0}}, \tag{21}$$

For the unloading case, the elastoplastic tangent matrix is identical to the elastic matrix.

5. Results and Discussions

This section is dedicated to simulate the seismic behavior of a soil profile under the influence of various factors under seismic loading. The methodology developed in the present study is applied to a soil column of 5m thickness above bedrock with $G_{base} = 200$ MPa, and $\rho = 2000\,\mathrm{kg/m^3}$. Figs. 5 and 6 schematize the elastic linear strain-hardening stress-strain behavior for the uniaxial case, and shear modulus variation with depth, respectively.

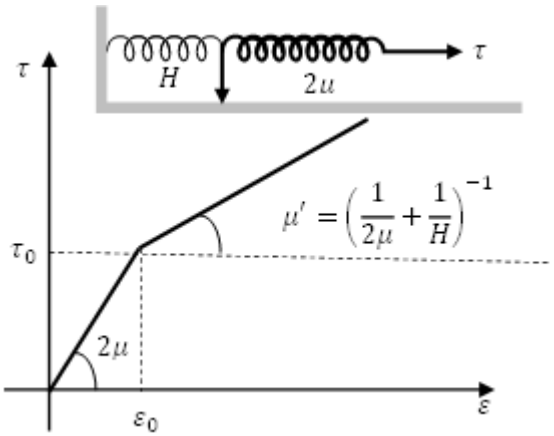

Fig. 5. Elastic, linear strain-hardening stress-strain behavior for the uniaxial case.

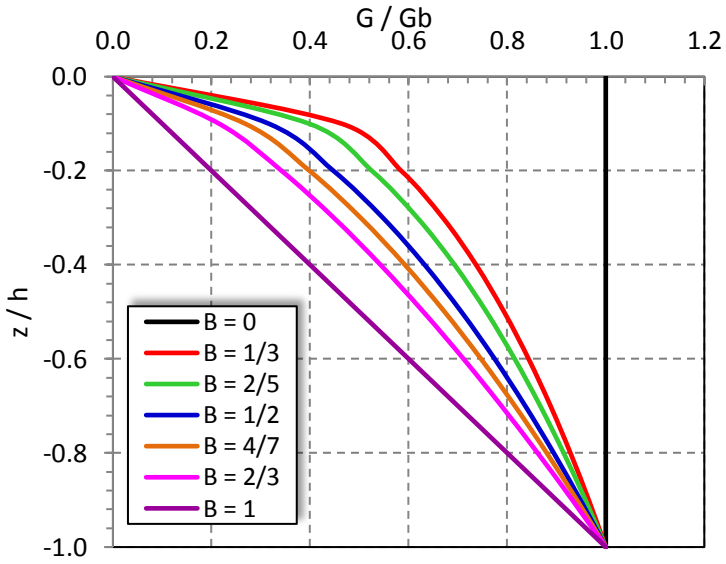

Fig. 6. Variation of shear modulus with depth.

The soil column is divided into five sublayers each one of 1m thickness. The response of the soil column is obtained in terms of depth-dependent displacements and accelerations as well as stress-strain hysteretic loop due to a vertical incident *SV* shear wave form the first order Ricker signal (Fig. 7).

Fig. 8 plots the depth-dependent distribution of maximum displacement along the soil column for different values of the parameter B in the nonlinear spatial variation of shear modulus. Fig. 9 shows the depth-dependent distribution of maximum acceleration with respect to that at the base of the soil profile (a_{max}/a_{base}). However Fig. 10 depicts the stress-strain hysteretic loop at the sublayer $n^{\circ}5$ due to the assumed degradation of shear modulus.

From Figs. 8 to 10, one may note the influence of the parameter B (power in the variation with depth of the shear modulus) on the predicted response. It expresses the key input step in the nonlinear response analysis of soils. On other hand, this shape of the hysteresis loop in Fig. 10 is controlled by its inclination and its breadth. The inclination of the loop depends on the stiffness (secant shear modulus) of the soil which decreases during the loading process. While the breadth of the hysteresis loop expresses the energy dissipation, commonly described by the damping ratio.

Another key parameter that controls the nonlinear response is the initial yield surface in terms of initial elastic strain as shown in Fig. 11(a) which depicts the depth-dependent distribution of maximum acceleration with respect to that at the base of the soil profile (a_{max}/a_{base}) for three assumptions of initial elastic strain. For the same assumptions, the stress-strain hysteretic loop is plotted in Fig. 11(b) at the level of the 5th sublayer.

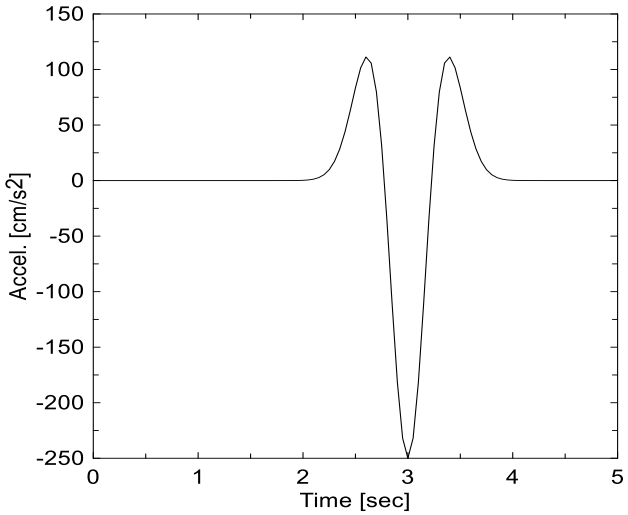

Fig. 7. Total acceleration time history at the base of the soil column.

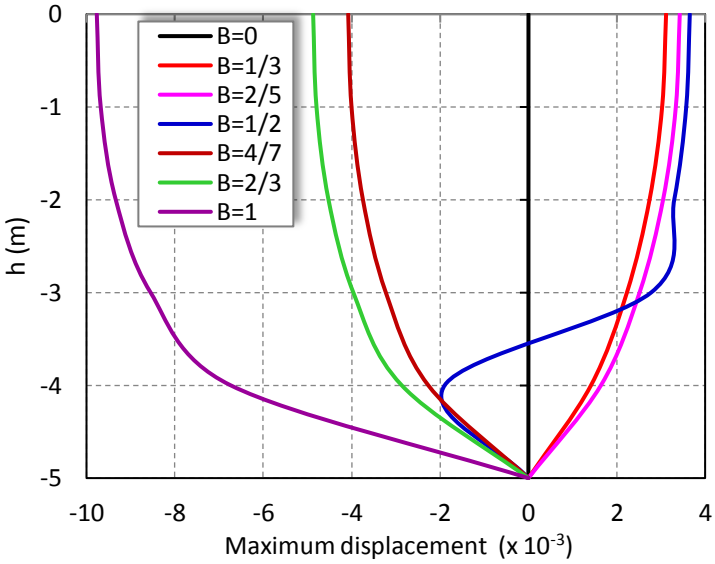

Fig. 8. Depth-dependent distribution of the maximum displacement along the soil profile.

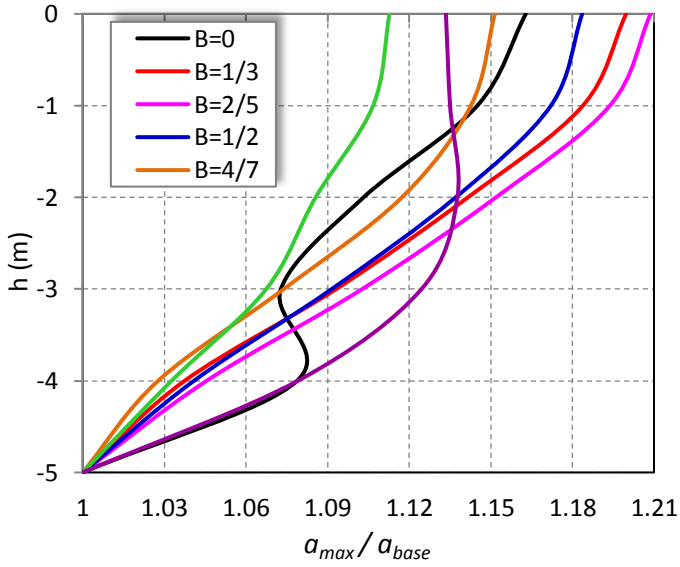

Fig. 9. Depth-dependent distribution of the maximum acceleration with respect to that at the base of the soil profile (a_{max}/a_{base}) along the soil profile.

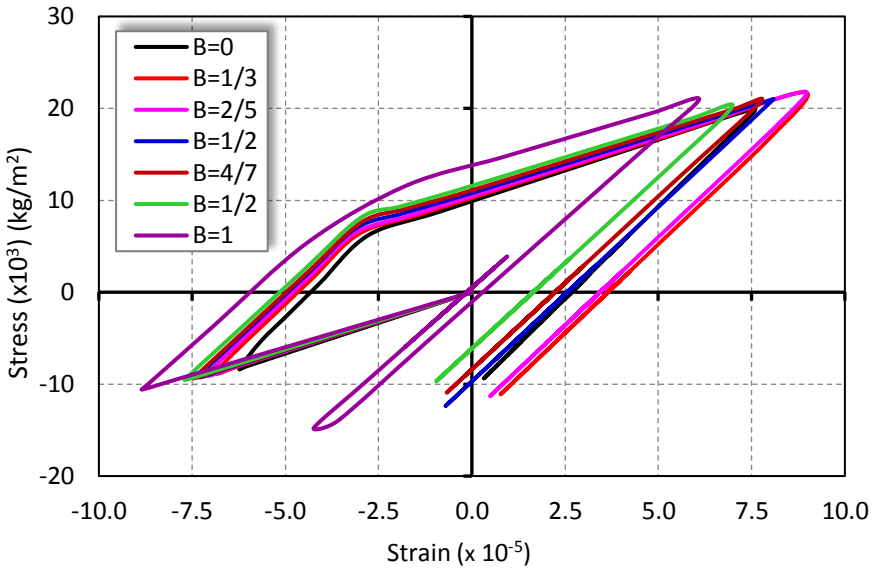

Fig. 10. Stress-strain hysteretic loop at sublayer number n°5.

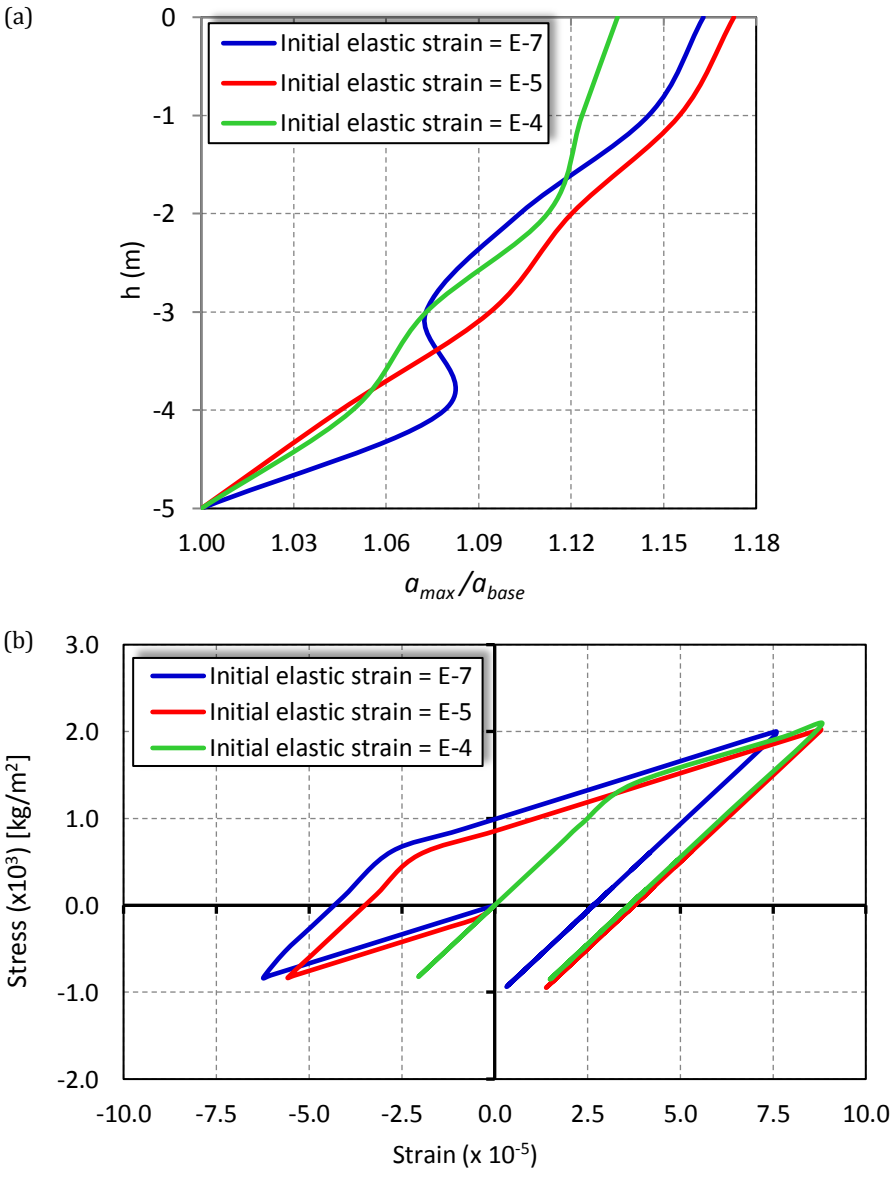

Fig. 11. Nonlinear responses of a soil profile for different initial yield surface: (a) ratio a_{max}/a_{base} ; (b) stress-strain hysteretic loop.

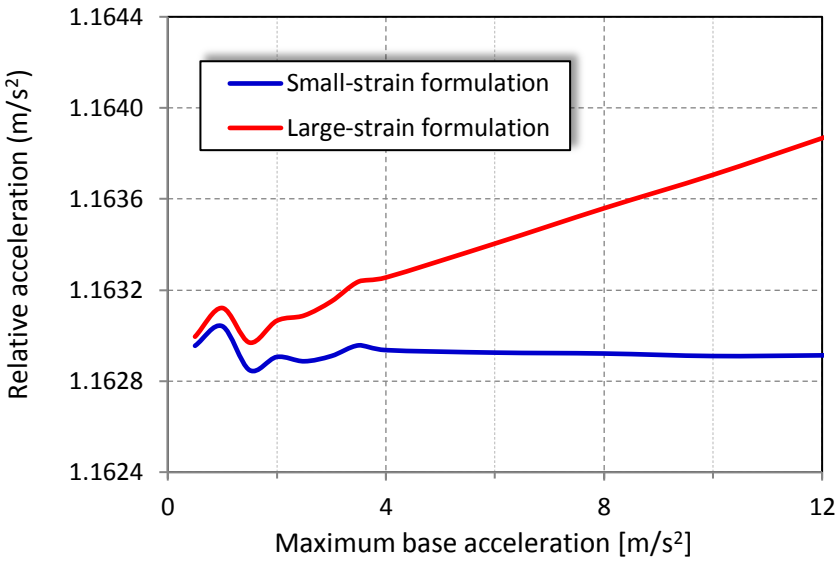

Fig. 12. Relative acceleration versus the maximum acceleration at the base of a soil profile for small- and large-strain formulations.

Under these conditions, both the inclination and the breadth of the loop are affected by the variation of the initial yield surface. So, to perfectly predict nonlinear soil responses, spatial variation of shear modulus together with material nonlinearity should be adequately selected according the each kind of material.

Finally, Fig. 12 shows the influence of the integration of the Von Mises elastoplastic equation according to small- and large-strain formulations. It compares the predicted soil responses in terms of relative accelerations of the soil profile versus maximal base acceleration using both small- and large-strain formulations. It is seen from Fig. 12, a large difference between the responses under the hypotheses of small- and large-strain formulations when the base acceleration (excitation) increases. However, deep interpretation of such behavior needs appropriate selection of the calculation method according to the solicitation level in the loading process, especially in the cases of seismic shaking.

6. Conclusions

The present study was principally dedicated to the development of a methodology to incorporate spatial and material variation of shear modulus in predicting the nonlinear responses of soil deposits under seismic excitations according to the incremental theory of plasticity. Moreover, the efficiency of the elastoplastic model using the Von Misès criterion in the prediction of the seismic responses was studied.

Firstly, the problem was formulated under the assumption of isotropic hardening in which the yield surface expands with plastic deformation, in the formwork of the FEM. Then, the equation of motion was integrated using the Newmark integration scheme. Lastly, a parametric study was conducted to show the influence of some parameters on the predicted responses.

This study showed that several factors considerably influence the nonlinear predicted seismic ground responses. The variation of the stiffness matrix due to the variation of the parameter B translating the spatial variation of the shear modulus leaded to large variations in the predicted nonlinear soil profile response in terms of depth-dependent distribution of the maximum displacement (Fig. 8) along the soil profile, maximum depth-dependent distribution of the maximum acceleration with respect to that at the base of the soil profile (Fig. 9), and stresses-strain hysteretic loop (Fig. 10). Also, the initial elastic strain affected the predicted responses (Fig. 11(a,b) because the evolution of the yield surface depends on these limits. Finally, the calculation method, i.e. small- or large-strain formulation also guided the predicted responses (Fig. 12).

So, accurate prediction of nonlinear seismic soil responses should adequately include spatial variation of soil properties such as shear modulus together with material nonlinearity for soil material. Furthermore, appropriate constitute equation and efficient integration scheme are required.

There is also the option to include a subheading within the Appendix if you wish.

References

Abdel-Ghaffar A, Koh AS (1981). Longitudinal vibration of non-homogeneous earth dams. *Earthquake Engineering and Soil Dynamics*, 9(3), 279-305.

Afra H, Pecker A (2002). Calculation of free field response spectrum of a nonhomogeneous soil deposit from bed rock response spectrum. *Soil Dynamics and Earthquake Engineering*, 22(2), 157–65.

Bathe KJ (1996). Finite Element Procedures. Library of Congress Cataloging-in-Publication Data.

Chopra A (2012). Dynamics of structures: Theory and applications to earthquake engineering. Prentice Hall.

Dakoulas P, Gazetas G (1985). A class of inhomogeneous shear models for seismic response of dams and embankments. *Soil Dynamics and Earthquake Engineering*, 4, 166-182.

Dunne F, Petrinic N (2006). Introduction to computational plasticity. Oxford University Press.

Elgamal AW (1991). Shear hysteretic elasto-plastic earthquake response of soil systems. *Earthquake Engineering and Structural Dynamics*, 20(4), 371-387.

Gu Q, Conte J P, Elgamal A, Yang Z (2009). Finite element response sensitivity analysis of multi-yield-surface J2 plasticity. *Computer Methods in Applied Mechanics and Engineering*, 198(30–32), 2272–2285.

Harichane Z, Chehat A, Sadouki A (2011a). Viscoelastoplastic earthquake shear hysteretic response of geomaterials. *Electronic Journal of Geotechnical Engineering*, 16 (Bund. M), 1566 -1582.

Harichane Z, Chehat A, Afra H (2011b). Post-elastic behavior of soil profiles under earthquake excitations. *Electronic Journal of Geotechnical Engineering*, 16 (Bund. P), 1471 -1485.

Harichane Z, Afra H, Bahar R (2012). Experimental validation of an identification procedure of soil profile characteristics from free field acceleration records. *International Journal of Geotechnical Earthquake Engineering*, 3(1), 1-17.

Hashash YMA, Park D (2001). Non-linear one-dimensional seismic ground motion propagation in the Mississippi embayment. *Engineering Geology*, 62(1–3), 185–206.

Hashash YMA, Park D (2002). Viscous damping formulation and high frequency motion propagation in non-linear site response analysis. *Soil Dynamics and Earthquake Engineering*, 22, 611-624.

Kaklamanos J, Baise LG, Thompson EM, Dorfmann L (2015). Comparison of 1D linear, equivalent-linear, and nonlinear site response models at six KiK-net validation sites. *Soil Dynamics and Earthquake Engineering*, 69, 207-219.

Khellafi MA, Harichane Z, Afra H, Sadouki A (2013). A case study of accelerometric records analysis of May 21st, 2003, Boumerdes (Algeria) earthquake. *International Journal of Geotechnical Earthquake Engineering*, 4(2), 34-52.

Mercado V, El-Sekelly W, Zeghaland M, Abdoun T (2015). Identification of soil dynamic properties through an optimization analysis. *Computers and Geotechnics*, 65, 175–186.

Pecker A (1995). Validation of small strain properties from recorded weak seismic motions. *Soil Dynamics and Earthquake Engineering*, 14(6), 399–408.

Stewart JP, Kwok AOL, Hashash YMA, Matasovic N, Pyke R, Wang Z, Yang Z (2008). Benchmarking of nonlinear geotechnical ground response analysis procedures. PEER Report 2008/04, University of California, Berkeley.

Vasileiois AD, Georolymos N, Gazetas G (2012). Constitutive model for soil amplification of ground shaking: Parameter calibration, comparisons, validation. *Soil Dynamics and Earthquake Engineering*, 42, 255–274.

Challenge Journal of Structural Mechanics

Flexural behavior of sustainable reactive powder concrete bubbled slab flooring elements

Ashraf Abdulhadi Alfeehan *, Hassan Issa Abdulkareem, Shahad Hameed Mutashar

Department of Civil Engineering, Al-Mustansiriyah University, 14022 Baghdad, Iraq

ABSTRACT

Voided slabs are reinforced concrete slabs in which voids allow to reduce the amount of concrete. The bubbled deck slab is a new and sustainable biaxial floor system to be used as a self-supporting concrete floor. The use of voided slabs leads to decrease the consumption of materials and improve the insulation properties for enhancing the objectives of sustainability. This study presents an investigation into the flexural behavior of sustainable Reactive Powder Concrete RPC bubbled slab flooring elements. Six one-way slabs were cast and tested up to the failure. The adopted variables in this study are: the volumetric ratio of steel fibers, type of slab; bubbled or solid, placing of reinforcement and thickness of slab. The effect of each variable on the ultimate load, deflection and strain has been discussed. The results show that increasing the percent of steel fibers from 1% to 2% in solid and bubbled slabs decreases the deflection by (18.75%) and (50%) respectively. As well as, the deflection increases by (41%) for bubbled slab compared to the solid slab. The slabs reinforced with top and bottom steel meshes show less deflection than slabs reinforced by only bottom steel mesh.

ARTICLE INFO

Article history:
Received 25 November 2016
Revised 13 March 2017
Accepted 7 April 2017

Keywords:
Reactive powder concrete
Voids
Bubbled slabs
Sustainability
Flooring elements

1. Introduction

Reinforced concrete slab is defined as the member that used in floors and roofs of buildings and as the decks of bridges. The floor system of a structure can take many forms such as in-situ solid slabs, ribbed slabs or precast units. Slabs may span in one direction or in two directions and they may be supported on monolithic concrete beams, steel beams, walls or directly by the structure's columns by Lee and Burnett (2008).

Sustainability means conserving natural resources and improving the quality of life for people through the use of natural resources and energy in a manner that enable the next generation to live in peace at the same time as the current generations are enjoying and not restricted (Clough et al., 2006; Ochsendorf, 2011; Cole et al., 2005).

Various attempts have been developed in the past to reduce the weight of concrete slabs, with maintaining the flexural strength of the slab. Reducing the slab weight would reduce deflection and make larger span lengths achievable. Not all the internal concrete can be replaced, where concrete in the top zone of the slab is necessary to form the compression block for flexural strength, and concrete in the tension zone of the slab needs to bond with reinforcement to make the reinforcement effective for flexural strength. Also, the top and bottom faces of the slab need to be connected to work as a one unit and ensure the transfer of the stresses (Mosley and Bungey, 2012; Marais, 2009).

The voided reinforced concrete slab system, also known as Bubbled Deck Slab system, has recently been presented in Europe. It was invented by Danish engineer, Jorgen Breuning. This system consists of hollow plastic balls cast into the concrete to create a grid of void forms inside the slab by Fuchs (2006) and Klein (2006).

Research over the past periods had yielded a new organization of highly resilient concrete called Reactive Powder Concrete (RPC), now labeled and classified as Ultra High Performance Concrete (UHPC). RPC is one of the latest generations in concrete technology by Therresa et al. (2008).

* *Corresponding author*. Tel.: +964-770-2682131 ; E-mail address: drce_ashrafalfeehan@uomustansiriyah.edu.iq (A. A. Alfeehan)
ISSN: 2149-8024 / DOI: https://doi.org/10.20528/cjsmec.2017.04.010

RPC possesses Ultra-high static and dynamic strength, high fracture capacity, low shrinkage and excellent durability under harsh conditions. The microstructure of RPC is improved by accurate gradation of all particles in the mix to achieve maximum compactness by Yunsheng et al. (2008).

2. Highlights

Minimization of the amount of concrete, providing the required span, overcoming concrete weakness in tension, monolithic and simple behavior with continuous and uniform forces distribution, enhancing heat and sound insulation etc. are the main reasons for the use of voided slabs. This paper presents an experimental study of the combination of the biaxial bubbled slabs technique with the use of reactive powder concrete as high performance concrete for sustainable roofing elements.

3. Experimental Program

Six, one-way RPC slabs with a rectangular cross-sectional area of (416mm) width, (100 and 125mm) depth and (1700mm) length were cast to study the effect of adopted parameters.

3.1. Materials of reactive powder concrete

RPC consists of the following materials shown in Table 1.

3.2. Materials for voided slabs

Materials listed in Table 2 are used in this experimental work for reinforcing and forming bubbled and solid slabs.

Table 1. Properties of materials of RPC.

Material	Property
Cement	Ordinary Portland Cement Type-I (AL-Maas) by Iraqi Specification, No. 5 (1984).
Sand	Natural sand from Al-Ukhaider region with maximum size of (600 μm) by Iraqi Specification, No.45 (1984), and B.S. 882. (1992).
Silica Fume	A gray colored material was produced by Sika Company, Turkey by ASTM C 1240 (2005).
Steel Fibers	Micro golden straight steel fibers of (13mm length and 0.22mm diameter).
Super Plasticizer	Glenium 51 manufactured by BASF Construction Chemicals, Jordan by ASTM C494 (2004).
Water	Ordinary tap water

Table 2. Materials for voided slabs.

Material	Property
Steel Bars	Deformed steel bars of (4mm diameter) having (560MPa) yield strength.
Balls	Plastic balls used were made by embodying high density polypropylene (HDPE) with a diameter of (75mm).

3.3. Mix proportion

Two mixes were used in this study with the same quantities and percentages of RPC components and two different ratios of micro steel fibers (1% & 2%) as shown in Table 3.

3.4. Preparation of bubbled slab

- Steel reinforcement layer of (4 mm) bar diameter and (50 mm × 50 mm) openings was placed in their correct position at the bottom with cover equal to (25mm).
- Balls of (75 mm) diameter were placed over the steel reinforcement layer at spacing of (25 mm) between balls in both transverse and longitudinal directions.
- For bubbled slab with bottom steel reinforcement only, the balls tied to the reinforcement layer by steel wire to prevent balls floating while concrete pouring.
- For bubbled slab with top and bottom steel reinforcement, the top reinforcement layer placed over the balls and then tied to the bottom layer by steel wire as shown in Fig. 1.

4. Specimen Details

Six rectangular RPC specimens were cast to study the flexural behavior of sustainable reactive powder concrete voided slabs. Details of slab specimens are shown in Table 4 and Figs. 2-3.

Table 3. Concrete mixes.

Cement kg/m³	Sand kg/m³	Silica Fume % of (cement weight)	w/c	Super Plasticizer % of (cementitious materials)	Steel Fiber %
1000	1000	8	0.25	6	1 & 2

Table 4. Details of tested slabs.

Slab Coding	Details
S-1-B-125	Solid Slab, 1% Steel Fiber, Bottom Reinforcement and 125 mm Thickness
S-2-B-125	Solid Slab, 2% Steel Fiber, Bottom Reinforcement and 125 mm Thickness
BS-1-B-125	Bubbled Slab, 1% Steel Fiber, Bottom Reinforcement and 125 mm Thickness
BS-1-TB-125	Bubbled Slab, 1% Steel Fiber, Top and Bottom Reinforcement and 125 mm Thickness
BS-2-TB-125	Bubbled Slab, 2% Steel Fiber, Top and Bottom Reinforcement and 125 mm Thickness
BS-1-TB-100	Bubbled Slab, 1% Steel Fiber, Bottom Reinforcement and 100 mm Thickness

Fig. 1. Preparation of bubbled slab.

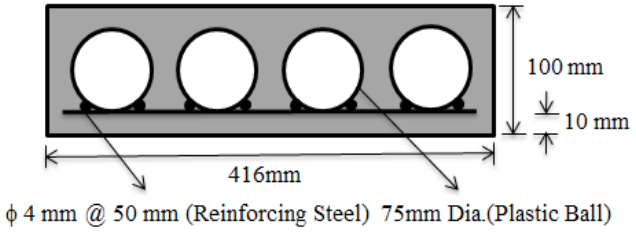

(a) Section of 100 mm thickness

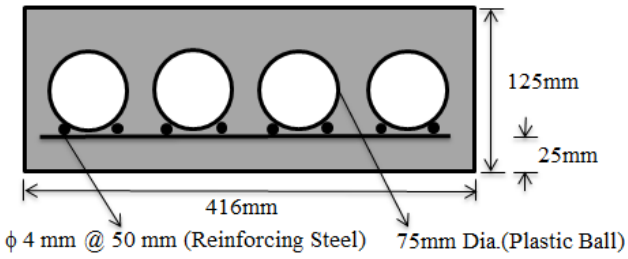

(b) Section of 125 mm thickness

Fig. 2. Front view of reinforced bubbled slab.

5. Test Instrumentation and Measurement

5.1. Load measurement

A universal hydraulic machine with (300 ton) capacity is used for specimens testing. All slabs were tested after (28) days as simply supported under two-point load, with a clear span of (500 mm) which is kept constant for all tests. The specimens are supported on steel rollers (50 mm) diameter. The load is distributed to two point loads by using steel blocks (40 mm thickness, 60 mm width and 416 mm length) which are placed on the top surface of the slab at both loading points to prevent local crushing of the concrete, as shown in Fig. 4. All tests were carried out under the condition of load step of (5 kN) for all specimens.

5.2. Deflection measurement

The deflection measurement is taken underneath midpoint. One dial gauge of (0.01mm) sensitivity is mounted on a steel frame was placed in the center of the bottom face of each specimen, as shown in Fig. 5.

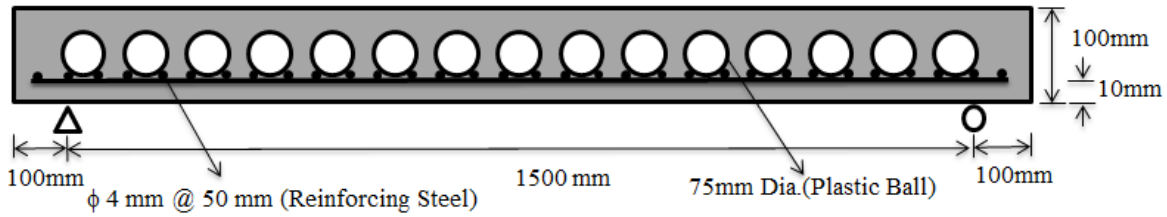

(a) Section of 100 mm thickness

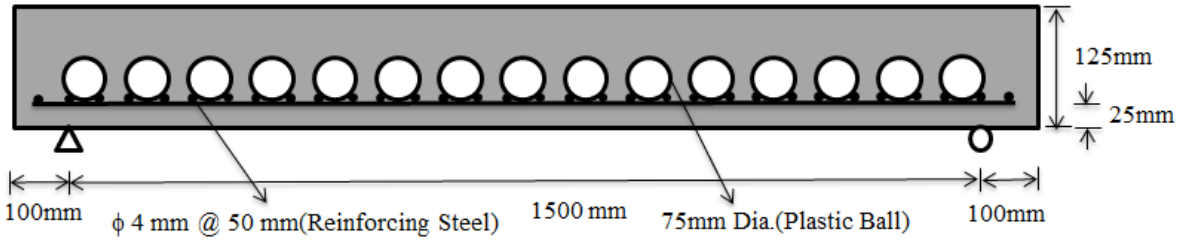

(b) Section of 125 mm thickness

Fig. 3. Side view of reinforced bubbled slabs.

Fig. 4. Preparation of testing slab specimen.

Fig. 5. Deflection measurement.

5.3. Concrete strain measurement

Concrete strain has been measured using electrical micro strains. Each specimen has two strain locations, the first in the center of the compression face (top surface) and the second in the center of the tension face (bottom surface). The strain wires were connected to a data logger instrument with movable ram memory for saving data and then transported to the computer in excel form.

6. Results and Discussion

As mentioned before, the objective of this paper is to study the flexural behavior of voided slab (bubbled slabs) made with RPC. Effects of steel fibers volumetric ratio, placing of reinforcement and type of slab on flexural behavior of RPC in terms of first cracking load, ultimate flexural load, maximum deflection, load-deflection and stress-strain curves were recorded and discussed below.

6.1. General behavior

RPC slabs tests showed that the general behavior of all slabs under flexural loading can be described as follows: at the early stage of loading, the first cracks appeared at the bottom of the mid span in the tension zone, the load in this stage is known as first crack load. With increasing loads, these cracks became wider and going upwards, also other cracks developed in the same zone. Further loading made the cracks to spread and extend faster; some of them reached the compression zone until the failure occurred at ultimate load capacity.

6.2. Load-deflection relationship

Deflection is measured at the center of the tension face of the tested slabs (at the mid span) by means of (0.01mm) dial gauges. The readings were recorded for each load increment. In general, the deflection increases linearly with the load in an elastic stage when the concrete slab is subjected to a gradual load increase. After the cracks start developing, deflection of the slab increases at a faster rate. After cracks have developed in the slab, the load-deflection curve is approximately linear up to the yielding of flexural reinforcement after which the deflection continues to increase without an appreciable increment in load. Table 5 shows the deflection values at the first and ultimate loading stages and Fig. 6 shows the load deflection curves of tested slabs at different loading stages.

Table 5. Deflection of first and ultimate cracking load.

Slab Coding	First Cracking Load (P_{cr}) kN	Cracking Deflection (Δ_{cr}) mm	Ultimate Load (Pu) kN	Ultimate Deflection (Δ_u) mm
S-1-B-125mm	25	1.8	78.5	18
S-2-B-125mm	42.5	2.1	87.5	35
BS-1-B-125mm	17.5	1.2	37.5	11.3
BS-1-TB-125mm	24	1.65	52.5	12.5
BS-2-TB-125mm	62.5	6.5	92.5	10.95
BS-1-TB-100mm	12.5	1.8	27.5	10.5

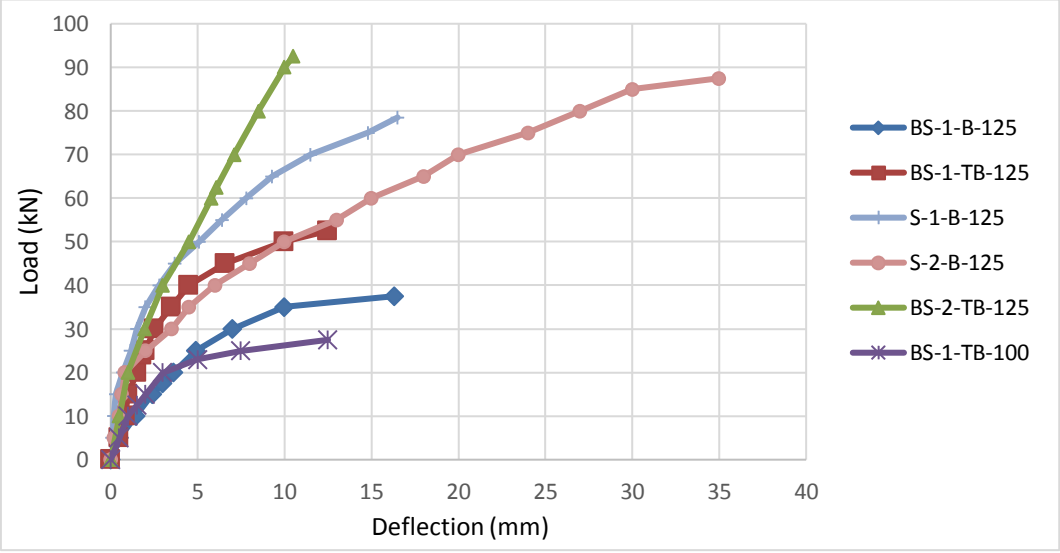

Fig. 6. Load-deflection relationship for tested slabs.

6.2.1. Effect of steel fiber ratios

The effect of the increasing steel fiber ratio from (1% to 2%) for solid slabs (S-1-B-125) & (S-2-B-125) of (125 mm) thickness with bottom reinforcement leads to increase the ultimate load capacity for slab (S-2-B-125) by (10%) and showing a significant increase in ductility while the deflection decreased by (18.75%) compared to slab (S-1-B-125) at the same stage of loading close to the first crack loading. Increasing the ratio of steel fiber in bubbled slabs (BS-1-TB-125) & (BS-2-TB-125) of (125 mm) thickness with top and bottom reinforcement lead to increase the ultimate load capacity for slab (BS-2-TB-125) by (43%) while the deflection decreases by (50%) compared to slab (BS-1-TB-125) as shown in Fig. 6. The increase in first crack and ultimate loads by increasing the steel fiber ratio results from restriction growing and expanding of the cracks also transition the tensile stress to concrete and surrounding cracks and result in increasing in load capacity.

6.2.2. Effect of voids

The presence of voids in slabs has great effect on ultimate load capacities and deflection values. The effect of bubbles in the slab (BS-1-B-125) compared with solid slab (S-1-B-125) with the same ratio of steel fiber, thickness and reinforcement decreases the ultimate load capacity by (52%) and the deflection by (41%) at the same stage of loading as shown in Fig. 6. The bubbled slab (BS-1-TB-100) has the least value of ultimate load (27.5 kN) as shown in Table 5 with minimum material used. By simple calculation, the equivalent distributed design live load that can be computed from the maximum applied moment is (12 kN/m^2) for the same slab length.

6.2.3. Effect of slab thickness

The increasing in thickness by 25% in slab (BS-1-TB-125) compared with slab (BS-1-TB-100) with 1% steel fiber ratio and same reinforcement led to increase the ultimate load capacity by (48%) while the deflection decreased by (40%) at the same stage of loading as shown in Fig. 6. The increase in deflection for a specimen of (100mm) thickness is caused by the reduction of stiffness which gives rise to a significant increase in deflection values.

6.2.4. Effect of steel reinforcement

The increase of reinforcing ratio, as well as the presence of compression reinforcement decreases the deflection and increase the load capacity. Although the slab is simply supported, the additional top steel for slab (BS-1-TB-125) contributes in increasing the ultimate load capacity by (29%) and decrease the deflection by (57%) compared to slab (BS-1-B-125) at the same stage of loading. This may be because of slightly increasing in the moment arm or by releasing of the top reinforcement role in the thin voided slab.

6.3. Stress-strain relationship

Concrete strain is measured by micro strain gauges which are placed in the center of tension and compression faces for each specimen. Fig. 7 shows the variation of strain for tested slabs at different loading stages and for compressive and tensile strains. It can be seen that the concrete compressive and tensile strain is small at the elastic stage as loading is applied, and then it increases after the first crack when loading is continued. Positive values in the diagrams refer to tension strain and negative values refer to compression strain. In most cases of reinforced concrete with high tensile steel fibers, the fiber does not reach to the ultimate strength and the failure occurs by pulling out the fibers.

6.3.1. Effect of steel fiber ratios

Fig. 7 shows that bubbled slab (BS-1-TB-125) and solid slab (S-1-B-125) have larger compressive and tensile strains than (BS-2-TB-125) and (S-2-B-125) respectively. This decrease in compressive and tensile strains attributed to the increasing in the percent of steel fibers from 1% to 2% would increase the bonding in bubbled and solid slabs with 2% than slabs with 1% steel fiber ratio and this lead to reduce strains in compression and tension.

6.3.2. Effect of voids

Bubbled slabs show compression and tensile strains larger than solid slab. The increase in strain for bubbled slab attributed to that the voids (balls) occupying significant space from the total volume. Lesser amount of concrete used in the bubbled slab than a solid slab leads to decrease the stiffness and increase the compression and tension strains as shown in Fig. 7.

6.3.3. Effect of slab thickness

The compression and tension strains increase when the thickness decreases from (125 to 100 mm) for bubbled slabs at the same stage of loading as shown in Fig. 7.

From the results of previous comparisons, it seems that the thickness has large effects mainly in each of the first cracking and ultimate loads, deformation and strains in both tension and compression.

6.3.4. Effect of steel reinforcement

The additional top reinforcement postpones the appearance of cracks and increases the ultimate load capacity, thereby the strains in compression and tension decreases in slabs of double reinforced.

6.4. Crack patterns and flexural failure mode of tested slabs

In general and for all the specimens, the cracks appear at the bottom surface of the concrete slabs and grow upward through loading stages. The first crack could not be

distinguished because it is internal crack and after seconds it appears in the middle of the slab and grows gradually across the width of the slab. Then the other cracks developed to the right and left of the first crack. Increasing the applied load, the displacement of slabs begins to increase at higher degree as more loads are applied and the ultimate crack occurs in the bottom face along the width of specimens. The ultimate failure crack shown in Fig. 8 and flexural failure modes of the slabs are shown in Figs 9(a-f).

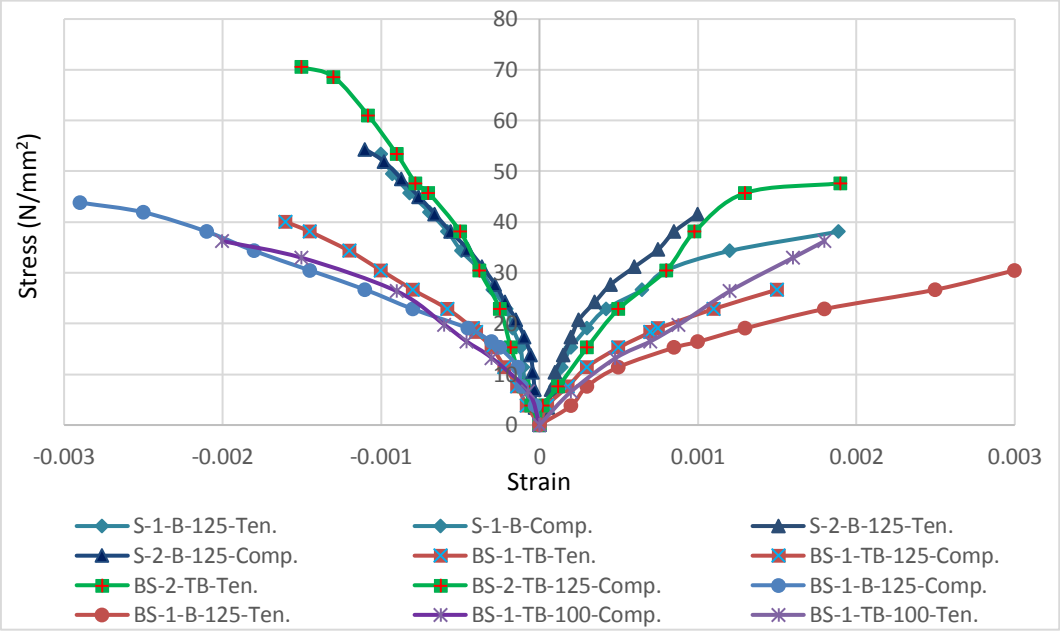

Fig. 7. Stress-strain diagram.

Fig. 8. Ultimate failure crack.

7. Conclusions

Biaxial voided slabs have many advantages over the conventional solid concrete slabs. Minimization of material, reduction of construction, lower cost, green technology, etc., are the main reasons for using these types of slabs. The effect of studied experimental parameters on the load capacity, strain and central deflection may be concluded as follows:

- The effect of the increasing steel fiber ratio improves the ultimate load capacity by (10%) for solid slabs with bottom reinforcement, while the ultimate load capacity increases by (43%) for bubbled slabs with top and bottom reinforcement.
- The deflection Influenced by increasing the steel fiber ratio from by (18.75%) for solid slabs with bottom reinforcement and by (50%) for bubbled slabs with top and bottom reinforcement.
- Increasing the thickness from 100 to 125 mm leads to increase the ultimate load capacity for bubbled slab with top and bottom reinforcement by (48%) while the deflection decreased by (40%).
- Additional top reinforcement in bubbled slabs improved the ultimate load capacity by (29%) and decreases the deflection by (57%).
- Bubbled slabs saving concrete by 18% compared to solid slab which reflects on the primary use of materials and CO2 emissions, so these slabs contribute the main objectives of sustainability.
- Increasing the steel fiber ratios from 1% to 2% shows improving the mechanical properties of RPC: f_{cu}, f'_c, f_{ct}, f_r and E_c by (16.88%, 17.63%, 50%, 39.4% and 11.12%) respectively.
- The study shows that this type of slabs satisfies the sustainability requirements and it is suitable for building which design live loads not exceed 12 kN/m^2.

(a) Flexural failure of (S-1-B-125mm)

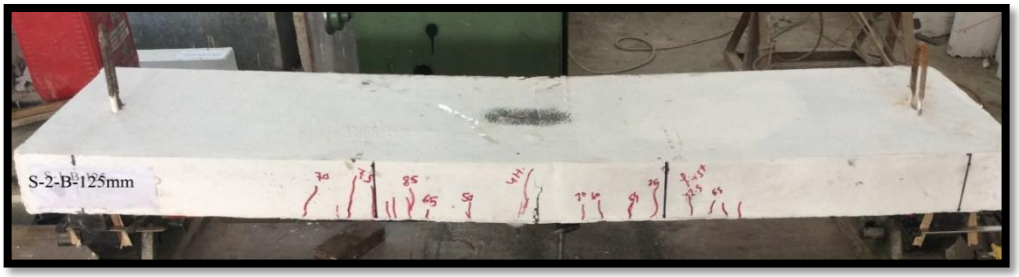

(b) Flexural failure of (S-2-B-125mm)

(c) Flexural failure of (BS-1-TB-125mm)

(d) Flexural failure of (BS-2-TB-125mm)

(e) Flexural failure of (BS-1-B-125mm)

(f) Flexural failure of (BS-1-TB-100mm)

Fig. 9. Flexural failure modes of the slabs.

Acknowledgements

Authors would like to thank Faculty of Engineering of Al-Mustansiriyah University, Baghdad, Iraq for the support to this research.

References

ASTM C494 (2004). Standard Specification for the Use of Super Plasticizer. American Society of Testing and Materials, Pennsylvania.

ASTM C1240 (2005). Standard Specification for the Use of Silica Fume as a Mineral Admixture in Hydraulic Cement Concrete. Mortar and Grout. Vol. 04.02., American Society of Testing and Materials, Pennsylvania.

BS 882 (1992). Specification for Aggregates from Natural Sources for Concrete, British Standard Institution.

Clough GW, Chameau JL, Carmichael C (2006). Sustainability and the University. *Presidency*, 9(1), 30-38.

Cole RJ, Nigel H, Ikaga T, Nibel S (2005). Building Environmental Assessment Tools: Current and Future Roles, In World Sustainable Building Conference.

Fuchs AC (2006). Technical Paper: BubbleDeck Span Guide. Bubble Deck Voided Flat Slab Solutions.

Iraqi Specification No. 5 (1984). Portland Cement, Ministry of Planning, Central Organization for Standardization and Quality Control.

Iraqi Specification, No. 45 (1984). Aggregate from Natural Sources for Concrete and Construction, Ministry of Planning, Central Organization for Standardization and Quality Control.

Klein D (2006). Structural Engineers, Sustainability and LEED. American Society of Civil Engineers.

Lee WL, Burnett J (2008). Benchmarking energy use assessment of HK-BEAM, BREEAM and LEED. *Building and Environment*, 43, 1882–1891.

Marais C (2009). Design Adjustment Factors and the Economical Applications of Concrete Flat-Slabs with Internal Spherical Voids in South Africa. *M.Sc. Thesis*, University of Pretoria.

Mosley WH, Bungey JH (2012). Reinforced Concrete Design, third edition, Macmillan.

Ochsendorf J, Norford LK, Brown D, Durschlag H, Hsu SL, Santero ALN, Swei O, Webb A, Wildnauer M (2011). Methods, Impacts, and Opportunities in the Concrete Building Life Cycle. Massachusetts Institute of Technology Concrete Sustainability Hub, Cambridge.

Therresa MA, Erron JP, Donald LM (2008) .Ultra High-Performance Concrete for Michigan Bridges Material Performance Phase-I, Center for Structural Durability. Michigan Technological Transpiration Institute.

Yunsheng Z, Wei S, Sifeng L, Chujie J, Jianzhong L (2008). Preparation of C200 green reactive powder concrete and its static dynamic behaviors. *Cement and Concrete Composites*, 30(9), 831–838.

Challenge Journal of Structural Mechanics

Teaching-learning based optimization for parameter estimation of double tuned mass dampers

Sinan Melih Niğdeli *, Gebrail Bekdaş

Department of Civil Engineering, İstanbul University, 34320 İstanbul, Turkey

ABSTRACT

The classical methods for parameter estimation of tuned mass dampers are well known simple formulations, but these formulations are only suitable for multiple degree of freedom structures by considering a single mode. If special range limitation of tuned mass dampers and inherent damping of the main structure are considered, the best way to estimate the parameters is to use a numerical method. The numerical method must have a good convergence and computation time. In that case, metaheuristic methods are effective on the problem. Generally, metaheuristic method is inspired from a process of life and it is formulated for several steps in order to reach an optimal goal. Differently from the single tuned mass dampers, double tuned mass dampers can be also used for the reduction of vibrations. In civil structures, earthquake excitation is a major source of vibrations. In this study, optimum double tuned mass dampers are investigated for seismic structures by using a wide range of earthquake records for global optimum. As an optimization algorithm, teaching learning based optimization is employed. In this algorithm, the teaching and learning phases of a class are modified for optimization problems. The optimization of double tuned mass damper is more challenging than the single ones since the number of design variable is doubled and the design constraint about the stroke of the both masses must be considered. The proposed method is compared with the existing approaches and the methodology is feasible for parameter estimation of double tuned mass dampers.

ARTICLE INFO

Article history:
Received 7 October 2016
Accepted 23 November 2016

Keywords:
Optimization
Teaching-learning based optimization
Double tuned mass dampers
Stroke capacity
Earthquakes

1. Introduction

In order to reduce mechanical vibrations, masses combined with stiffness and damping elements can be used. The name of this device is tuned mass damper (TMD) and initial form without inherent damping is invented by Frahm (1911). For random vibrations, Ormondroyd and Hartog (1928) implemented inherent damping to initial form. For that reason, TMDs are effective in the reduction of vibrations resulting from excitations with random frequency. Thus, TMDs are used in civil structures in order to reduce vibrations resulting from wind and earthquakes. In the optimum tuning of TMDs, closed form expressions are proposed but these formulas are for single degree of freedom systems (Hartog, 1947; Warburton, 1982; Sadek et al., 1997). By idealization of multiple degree of freedom systems, only a vibration mode can be used in finding TMD parameters. In the passive structural control of structures by using tuned mass dampers (TMDs), optimum parameters are depended to several factors such as excitations, soil characteristics, support conditions and TMD stroke capacity. Thus, numerical algorithms can be used and metaheuristic methods inspired by natural happenings are very effective for tuning problem.

In search of optimum parameters of TMDs for structures, metaheuristic algorithms have been employed. Metaheuristic algorithms are inspired from natural happenings such as natural evolution for Genetic Algorithm (GA) (Holland, 1975; Goldberg, 1989), swarm intelligence

* *Corresponding author*. Tel.: +90-212-4737070 ; Fax: +90-212-4737180 ; E-mail address: melihnig@istanbul.edu.tr (S. M. Niğdeli)
ISSN: 2149-8024 / DOI: https://doi.org/10.20528/cjsmec.2016.11.032

for Particle Swarm Optimization (PSO) (Kennedy and Eberhart, 1995), behavior of ants for Ant Colony (ACO) Algorithm (Dorigo et al., 1996), musical performances for Harmony Search (HS) (Geem et al., 2001) and education in teaching learning based optimization (TLBO) (Rao et al., 2011). Hadi and Arfiadi (1998) employed GA for optimum design of TMDs positioned on multiple degree of freedom (MDOF) seismic structures. By employing GA, Marano et al. (2010) optimized TMD parameters including the mass ratio instead of using a preselected mass for TMD. Additionally, GA has been employed in several TMD optimization methods (Singh et al., 2002; Desu et al., 2006; Pourzeynali et al., 2007). PSO was also employed for the TMD problem and several closed form expressions were obtained (Leung and Zhang, 2009; Leung et al., 2008). Steinbuch (2011) employed bionic optimization for estimating the best design of TMDs for earthquake resistance of structures. HS algorithm has been widely used in optimum design of TMDs (Bekdaş and Nigdeli, 2011; Bekdaş and Nigdeli, 2013) including prevention of brittle fracture (Nigdeli and Bekdaş, 2013). Farshidianfar and Soheili investigated optimum TMD design of structures including soil-structure interaction (SSI) by using several metaheuristic algorithms like ant colony optimization (Farshidianfar and Soheili, 2013a), artificial bee colony optimization (Farshidianfar and Soheili, 2013b) and shuffled complex evolution (Farshidianfar and Soheili, 2013c). TLBO is also used in parameter estimation of TMDs for seismic structures (Nigdeli and Bekdas, 2015a).

An important factor is the stroke capacity of TMDs. The optimum design variables may be different for a TMD system if stroke capacity is taken as a design constraint. In the study of Tributsch and Adam (2012), it is indicated that a TMD with a damping coefficient larger than the optimum one reduces maximum deflection of the TMD spring. For that reason, the stroke capacity is an effective factor for the optimum TMD properties and optimization is important in order to find a balance between performance and stroke capacity of TMD. Additionally, an energy-based theoretical model (Miranda, 2005), a damping maximized TMD (Miranda, 2012), close-form design formulas for random loads (Tigli, 2012) and Minimax optimization (Salvi and Rizzi, 2014) for TMDs have been proposed.

Another concept in passive vibration control is to use double tuned mass dampers (DTMDs) for seismic structures (Li and Zhu, 2006). Harmony search algorithm is employed in the optimization of DTMDs (Bekdaş and Nigdeli, 2014). Then, a multi-objective optimization is proposed for DTMDs employing HS and considering maximum stroke capacity of dampers (Nigdeli and Bekdaş, 2015b).

In this paper, TLBO optimization is employed for multi-objective optimization of DTMD parameters. The two objectives are the reduction of maximum top story displacement to a user defined value and the consideration of the stroke capacity by using a scaled displacement value of DTMD.

2. Methodology

A shear building with a DTMD is represented in Fig. 1. A single degree is defined for all stories and the number of the stories is defined by N. The equation of motion of the shear building subjected to ground acceleration is written as

$$M\ddot{x}(t) + C\dot{x}(t) + Kx(t) = -M\{1\}\ddot{x}_g(t)\,. \tag{1}$$

The M, C and K matrices are shown as Eqs. (2)-(4) and these matrices are diagonal lumped mass, damping and stiffness matrices, respectively. and these matrices are given in Eqs. (2)-(4). In the equations, $x(t)$, and {1} are a vector containing structural displacements of all stories and DTMD (as shown as Eq. (5)), ground acceleration and a vector of ones with a dimension of (N+2, 1), respectively.

$$\mathrm{M} = diag[m_1 m_2 \dots m_N m_{d1} m_{d2}]\,, \tag{2}$$

$$\mathrm{C} = \begin{bmatrix} (C_1+C_2) & -C_2 & & & & & \\ -C_2 & (C_2+C_3) & -C_3 & & & & \\ & \ddots & \ddots & \ddots & & & \\ & & & -C_N & (C_N+C_{d1}) & -C_{d1} & -C_{d2} \\ & & & & -C_{d1} & (C_{d1}+C_{d2}) & -C_{d2} \\ & & & & & -C_{d2} & -C_{d2} \end{bmatrix}, \tag{3}$$

$$\mathrm{K} = \begin{bmatrix} (k_1+k_2) & -k_2 & & & & & \\ -k_2 & (k_2+k_3) & -k_3 & & & & \\ & \ddots & \ddots & \ddots & & & \\ & & & -k_N & (k_N+k_{d1}) & -k_{d1} & -k_{d2} \\ & & & & -k_{d1} & (k_{d1}+k_{d2}) & -k_{d2} \\ & & & & & -k_{d2} & -k_{d2} \end{bmatrix}. \tag{4}$$

The symbols; m_i, c_i, k_i and x_i represents mass, damping coefficient, stiffness coefficient and displacement of i_{th} storey of structure. The parameters related with DTMD are masses (m_{d1}, m_{d2}), damping coefficients (c_{d1}, c_{d2}) and stiffness coefficients (k_{d1}, k_{d2}). The displacements of the DTMD are represented with x_{d1} and x_{d2}.

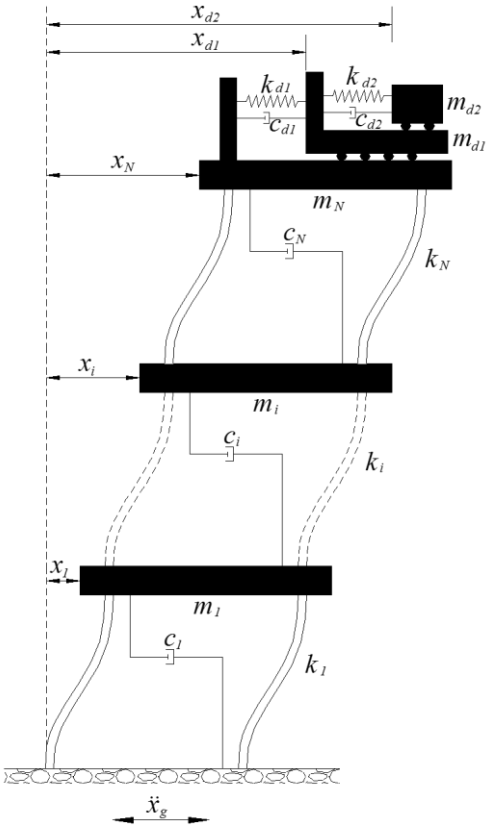

Fig. 1. Model of N-story shear building with a DTMD.

3. Teaching-Learning Based Optimization and Multi-Objective Optimization Methodology

TLBO algorithm uses two phases of the education process. These phases are called teacher and learner phases. TLBO consequently uses these phases without using a parameter in choose of the optimization type. This is a major advantage and difference of the algorithm.

As all methodologies using metaheuristic algorithms, structural properties, external excitations and ranges of design variables are defined. Then, the structure without DTMD is analyzed and the structural responses are obtained for all earthquake excitations. The objective functions are defined as Eqs. (5) and (6) and the stroke capacity objective defined by Eq. (6) contains responses of the structure without TMD. In these objectives, user defined values; x_{max} and *st_max* are the desired values for maximum displacement and stroke. If the user defined value of x_{max} is not applicable, the value is iteratively increased. Thus, x_{max} can be defined as zero for the minimization of the maximum displacement.

Before the iterative optimization process, an initial solution matrix must be generated. The vectors of the initial matrix are assigned with randomly generated design variables. The number of these vectors is equal to the population of the class. Then, teacher phase is started and existing design variables are updated by using the existing best solution as a teacher. In this phase, randomly defined teacher factor (1 or 2) is used in order to control the range of the new generation around the mean of the existing results. After the teacher phase, the student phase starts in order to improve the all existing solutions in solution matrix. In this generation, new solutions are obtained according to two existing solutions which are randomly chosen. These phases are formulized in Rao et al. (2011).

The modification of existing solutions with the new ones is done as follows. First, the objective function given as Eq. (6) is considered and if it is lower than *st_max*, the objective function is taken into consideration. The process of teacher and learner phases continue until the criteria are provided.

$$|x_N| \leq x_{max}\,, \tag{5}$$

$$max\left[\frac{max\ [\![x_{N+2}-x_{N+1}]\!]_{with\ DTMD}}{max\ [\![x_N]\!]_{without\ DTMD}}, \frac{max\ [\![x_{N+1}-x_N]\!]_{with\ DTMD}}{max\ [\![x_N]\!]_{without\ DTMD}}\right] \leq st\_max\,, \tag{6}$$

In the learner phase of TLBO algorithm, if the duplicate solutions exist, the algorithm may be trap to a local optimum. In order to avoid trapping, an elitist teaching learning based optimization (ETLBO) is developed by Rao and Patel (2012). In ETLBO, the duplicate solutions are modified by generated randomly selected solutions as done in the generation of initial solutions. In this paper, TLBO and ETLBO results are presented.

4. Numerical Examples

An optimum DTMD design is investigated for a ten story structure. The mass, stiffness coefficient and damping coefficient of a story are 360 t, 6.2 MNs/m and 650 MN/m, respectively (Singh et al., 2002). FEMA P-695 (2009) far-fault ground motion set (shown in Table 1) was used in the optimization process.

Two cases for the *st_max* limitation is investigated and *st_max* was taken as 0.8 and 1 for Case 1 and 2, respectively. The possible maximum reduction of the structural displacements is targeted. The same optimization is also done by using HS (Nigdeli and Bekdaş, 2015b).

The ranges for the design variables such as masses, periods and damping ratios of DTMD are between 0.1% and 5% of total mass of the structure, between 0.5 and 1.5 times of the critical period of the structure and between 1% and 30%, respectively. The optimum DTMD parameters (for HS, TLBO and ETLBO approaches) are given in Table 2. The performance of DTMD on reduction of structural displacements is discussed in the conclusions.

5. Conclusions

The optimum results are found according to the critical excitation of 44 far-field excitations and the BOL090 component of Düzce record of Düzce earthquake is the critical one. For the structure without DTMD, the maximum displacement of the structure is 0.4101 m. By using the stroke capacity of Case 1, this value is reduced to

0.2771 m, 0.2882 m and 0.2760 m for HS, TLBO and ETLBO, respectively. TLBO algorithm trap to a local region for Case 1. Thus, ETLBO is effective in obtaining the best results. The maximum displacements are 0.2626 m (HS), 0.2509 m (TLBO) and 0.2508 m (ETLBO) for Case 2. The effectiveness of TLBO and ETLBO is similar for the second case since the restriction of the stroke is low. In Fig. 2, the first and top storey displacement plots are shown for the first case of DTMD for ETLBO approach results.

According to the results, the methodology employing TLBO can trap to local optimum results. For that reason, ETLBO is an effective modification of the method. The proposed method for the optimization of DTMDs is suitable and global optimum results can be effectively found if the elitist version of TLBO is used.

Table 1. FEMA P-695 far-field ground motion records.

Earthquake Number	Date	Name	Component 1	Component 2
1	1994	Northridge	NORTHR/MUL009	NORTHR/MUL279
2	1994	Northridge	NORTHR/LOS000	NORTHR/LOS270
3	1999	Duzce, Turkey	DUZCE/BOL000	DUZCE/BOL090
4	1999	Hector Mine	HECTOR/HEC000	HECTOR/HEC090
5	1979	Imperial Valley	IMPVALL/H-DLT262	IMPVALL/H-DLT352
6	1979	Imperial Valley	IMPVALL/H-E11140	IMPVALL/H-E11230
7	1995	Kobe, Japan	KOBE/NIS000	KOBE/NIS090
8	1995	Kobe, Japan	KOBE/SHI000	KOBE/SHI090
9	1999	Kocaeli, Turkey	KOCAELI/DZC180	KOCAELI/DZC270
10	1999	Kocaeli, Turkey	KOCAELI/ARC000	KOCAELI/ARC090
11	1992	Landers	LANDERS/YER270	LANDERS/YER360
12	1992	Landers	LANDERS/CLW-LN	LANDERS/CLW-TR
13	1989	Loma Prieta	LOMAP/CAP000	LOMAP/CAP090
14	1989	Loma Prieta	LOMAP/G03000	LOMAP/G03090
15	1990	Manjil, Iran	MANJIL/ABBAR--L	MANJIL/ABBAR—T
16	1987	Superstition Hills	SUPERST/B-ICC000	SUPERST/B-ICC090
17	1987	Superstition Hills	SUPERST/B-POE270	SUPERST/B-POE360
18	1992	Cape Mendocino	CAPEMEND/RIO270	CAPEMEND/RIO360
19	1999	Chi-Chi, Taiwan	CHICHI/CHY101-E	CHICHI/CHY101-N
20	1999	Chi-Chi, Taiwan	CHICHI/TCU045-E	CHICHI/TCU045-N
21	1971	San Fernando	SFERN/PEL090	SFERN/PEL180
22	1976	Friuli, Italy	FRIULI/A-TMZ000	FRIULI/A-TMZ270

Table 2. The ranges of design variables and optimum values (DTMD).

Design variable	HS		TLBO		ETLBO	
	Case 1	Case 2	Case 1	Case 2	Case 1	Case 2
Mass (t)	160.18-169.56	178.64-173.16	180-180	179.50-179.82	164.34-180	179.51-179.79
Period (s)	0.5666-0.6775	0.6399-0.7077	0.5669-0.4946	0.6519-0.6710	0.5819-0.7947	0.6521-0.6677
Damping ratio (%)	28.28-18.68	28.88-9.35	30-1	26.31-1	27.64-27.44	26.26-1

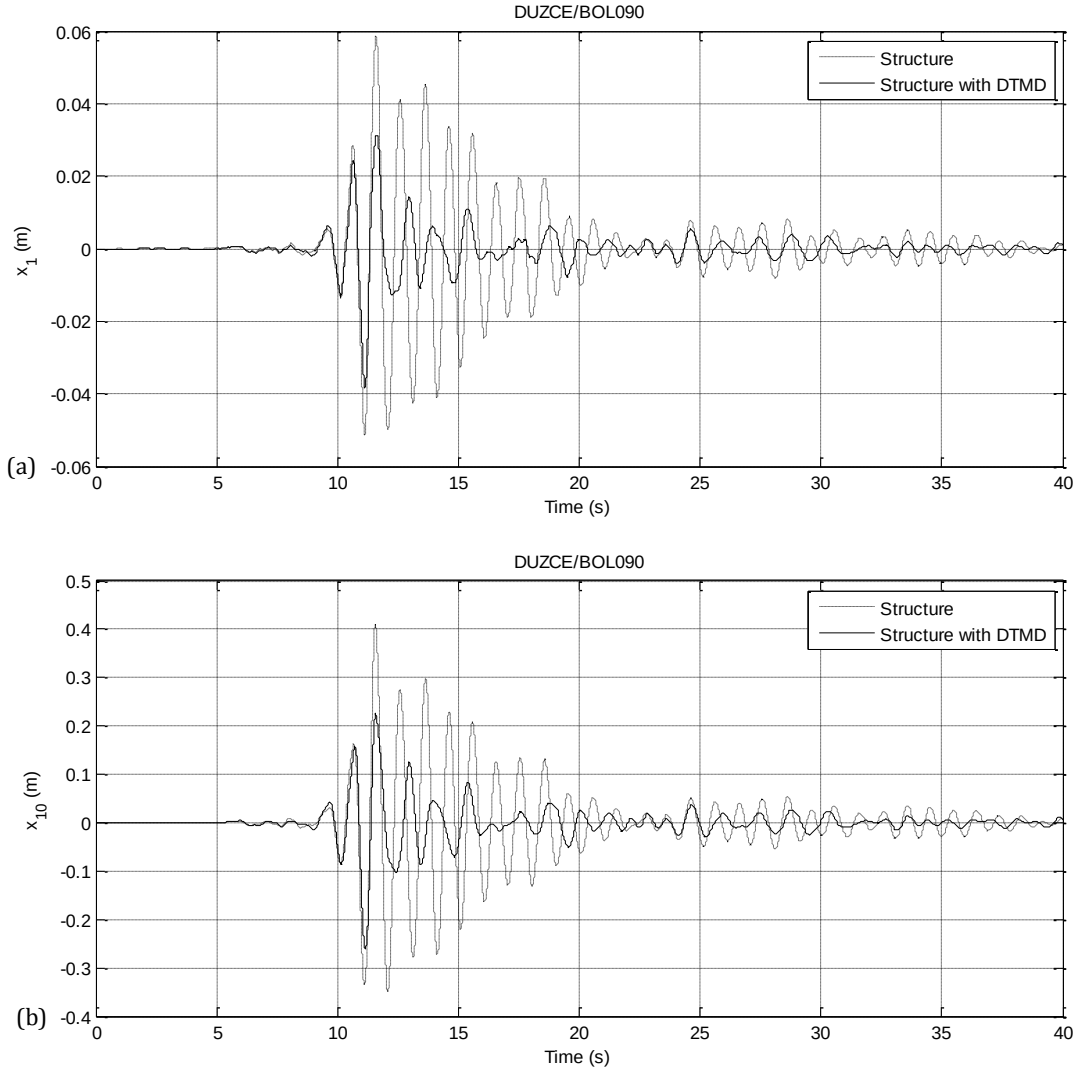

Fig. 2. The time history plots for the critical excitation: (a) CASE 1; (b) ETLBO.

REFERENCES

Bekdaş G, Nigdeli SM (2011). Estimating optimum parameters of tuned mass dampers using harmony search. *Engineering Structures,* 33, 2716–2723.

Bekdaş G, Nigdel SM (2013). Mass ratio factor for optimum tuned mass damper strategies. *International Journal of Mechanical Sciences,* 71, 68–84.

Bekdaş G, Nigdeli SM (2014). Optimization of double tuned mass dampers by using harmony search. *The 12th International Conference on Computational Structures Technology*, September 2-5, Naples, Italy.

Den Hartog JP (1947). Mechanical Vibrations. McGraw-Hill, New York.

Desu NB, Deb SK, Dutta A (2006). Coupled tuned mass dampers for control of coupled vibrations in symmetric buildings. *Structural Control and Health Monitoring*, 13, 897–916.

Dorigo M, Maniezzo V, Colorni A (1996). The ant system: Optimization by a colony of cooperating agents, *IEEE Transactions on Systems Man and Cybernet*, B 26, 29–41.

Farshidianfar A, Soheili S (2013a). Ant colony optimization of tuned mass dampers for earthquake oscillations of high-rise structures including soil-structure interaction. *Soil Dynamics and Earthquake Engineering*, 51, 14-22.

Farshidianfar A, Soheili S (2013b). ABC optimization of TMD parameters for tall buildings with soil structure interaction. *Interaction and Multiscale Mechanics*, 6(4), 339–356.

Farshidianfar A, Soheili S (2013c). Optimization of TMD parameters for earthquake vibrations of tall buildings including soil structure interaction. *International Journal of Optimization in Civil Engineering*, 3, 409–429.

FEMA P-695 (2009). Quantification of Building Seismic Performance Factors. Federal Emergency Management Agency, Washington DC.

Frahm H (1911). Device for Damping of Bodies. U.S. Patent No: 989, 958.

Geem ZW, Kim JH, Loganathan GV (2001). A new heuristic optimization algorithm: harmony search, *Simulation*, 76, 60–68.

Goldberg DE (1989). Genetic Algorithms in Search, Optimization and Machine Learning. Boston MA: Addison Wesley.

Hadi MNS, Arfiadi Y (1998). Optimum design of absorber for MDOF structures. *Journal of Structural Engineering-ASCE*, 124, 1272–1280.

Holland JH (1975). Adaptation in Natural and Artificial Systems. Ann Arbor MI: University of Michigan Press.

Kennedy J, Eberhart RC (1995). Particle swarm optimization. *Proceedings of IEEE International Conference on Neural Networks No. IV*, Perth Australia; November 27-December 1, 1942–1948.

Leung AYT, Zhang H, Cheng CC and Lee YY (2008). Particle swarm optimization of TMD by non-stationary base excitation during earthquake. *Earthquake Engineering and Structural Dynamics*, 37, 1223–1246.

Leung AYT and Zhang H (2009). Particle swarm optimization of tuned mass dampers. *Engineering Structures*, 31, 715-728.

Li C, Zhu B (2006). Estimating double tuned mass dampers for structures underground acceleration using a novel optimum criterion. *Journal of Sound and Vibration*, 298, 280–297.

Marano GC, Greco R, Chiaia B (2010). A comparison between different optimization criteria for tuned mass dampers design. *Journal of Sound and Vibration*, 329, 4880-4890.

Miranda JC (2005). On tuned mass dampers for reducing the seismic response of structures. *Earthquake Engineering and Structural Dynamics*, 34, 847–865.

Miranda JC (2012). System intrinsic, damping maximized, tuned mass dampers for seismic applications. *Structural Control Health Monitoring*, 19, 405–416.

Nigdeli SM, Bekdaş G (2013). Optimum tuned mass damper design for preventing brittle fracture of RC buildings. *Smart Structures and Systems*, 12(2), 137–155.

Nigdeli SM, Bekdaş G (2015a). Teaching-Learning-Based optimization for estimating tuned mass damper parameters. *3rd International Conference on Optimization Techniques in Engineering (OTENG '15)*, November 7–9, Rome, Italy.

Nigdeli SM, Bekdaş G (2015b). Multi objective optimization of double tuned mass dampers considering maximum stroke capacity. *International Conference on Engineering Vibration*, September 7–10, Ljubljana, Slovenia.

Ormondroyd J, Den Hartog JP (1928). The theory of dynamic vibration absorber. *Transactions of the American Society of Mechanical Engineers*, 50, 9–22.

Pourzeynali S, Lavasani HH, Modarayi AH (2007). Active control of high rise building structures using fuzzy logic and genetic algorithms. *Engineering Structures*, 29, 346-357.

Rao RV, Savsani VJ, Vakharia DP (2011). Teaching–learning-based optimization: a novel method for constrained mechanical design optimization problems. *Computer-Aided Design*, 43(3), 303–315.

Rao R, Patel V (2012). An elitist teaching-learning-based optimization algorithm for solving complex constrained optimization problems. *International Journal of Industrial Engineering Computations*, *3*(4), 535–560.

Sadek F, Mohraz B, Taylor AW, Chung RM (1997). A method of estimating the parameters of tuned mass dampers for seismic applications. *Earthquake Engineering and Structural Dynamics*, 26, 617–635.

Salvi J, Rizzi E (2014). Optimum tuning of Tuned Mass Dampers for frame structures under earthquake excitation. *Structural Control Health Monitoring*, 22(4), 707–725.

Steinbuch R (2011). Bionic optimisation of the earthquake resistance of high buildings by tuned mass dampers. *Journal of Bionic Engineering,* 8, 335–344.

Singh MP, Singh S, Moreschi LM (2002). Tuned mass dampers for response control of torsional buildings. *Earthquake Engineering and Structural Dynamics*, 31, 749–769.

Tigli OF (2012). Optimum vibration absorber (tuned mass damper) design for linear damped systems subjected to random loads. *Journal of Sound and Vibration*, 331(13), 3035–3049.

Tributsch A, Adam C (2012). Evaluation and analytical approximation of Tuned Mass Damper performance in an earthquake environment. *Smart Structures and Systems,* 10(2), 155–179.

Warburton GB, (1982). Optimum absorber parameters for various combinations of response and excitation parameters. *Earthquake Engineering and Structural Dynamics*, 10, 381–401.

Challenge Journal of Structural Mechanics

The strain sensitivity of copper powder reinforced concrete

Egemen Teomete *, Özkan Ayberk Kolatar, Erman Demircilioğlu, Serap Kahraman

Department of Civil Engineering, Dokuz Eylül University, 35160 İzmir, Turkey

ABSTRACT

Earthquakes, material deteriorations and other environmental factors challenge the structural safety. In order to protect the lives, structural health monitoring is crucial. The metal foil strain gages have low durability, low sensitivity and can get point wise measurements which are disadvantages. In this study six different concrete mixtures were designed; one without any copper powder, the rest five having different copper powder volume fractions. Three cube samples from each mixture were cast and cured. Simultaneous measurement of electrical resistance and strain were conducted during the compression tests. A strong linear relationship between strain and electrical resistance change was obtained for copper powder reinforced concrete. The results are contribution to the development of "Smart Concrete" which can sense its strain and damage.

ARTICLE INFO

Article history:
Received 6 February 2017
Accepted 25 February 2017

Keywords:
Smart concrete
Self-sensing
Electrical resistance
Compression test
Smart structures
Copper powder

1. Introduction

Material degradations, earthquakes and other environmental factors challenge the structures. Concrete infrastructures are deteriorated before the design life and 30% of bridges were reported to be structurally deficient (Reza et al., 2003). For this reason structural health monitoring is an important task. One of the widely used sensors in structural health monitoring is metal foil strain gages. Metal foil strain gages have low durability, low sensitivity and high cost. These properties of metal foil strain gages restrict their use for a long time and in vast numbers (Chung, 2001). Self-sensing smart concrete is an ideal engineering material for satisfying this issue.

Relation between electrical resistance change and compressive strain for copper powder reinforced concrete was investigated in this project. Copper powder was used as a conductive phase in the concrete mix due to its good electrical characteristic. Addition of carbon fibers in cement matrix decreases its electrical resistance. Under strain, electrical resistance of carbon fiber reinforced cement composites changes (Chung, 1998; Fu et al., 1997). Addition of carbon fiber in cement matrix improves tensile strength, ductility and flexural strength while decreasing shrinkage cracking (Chung, 2000). Different test setups and electrode configurations were tested in determining the strain sensitivity of carbon fiber reinforced cement composites (Chiarello and Zinno, 2005; Han et al., 2007; Reza et al., 2004; Chen and Liu, 2008). The sample cross section and the distance between the electrodes affect the resistance measurements in two electrode method while they do not have an effect on four electrode method. Four electrode method is preferred as it gives more accurate results (Chiarello and Zinno, 2005; Han et al., 2007). Under compressive load, the fibers are under compression during loading so the electrical resistance decreases. Loading will develop damage in the material which will change the electrical resistance (Chung, 2000). Strain sensing, crack detection and damage assessment of concrete structures can be achieved by the carbon fiber reinforced cement based composites (Teomete, 2015).

In this study, different volume fractions of copper powder were used in the mix design of concrete. Four electrode method was used at the tests. The strain and electrical resistance of the samples were simultaneously measured during compression test. The electrical resistance change - strain correlations were determined. Gage factor, linearity and strain limit which are performance measures of a strain gage were determined for the copper powder reinforced smart concretes.

* *Corresponding author*. Tel.: +90-232-3017060 ; Fax: +90-232-4531192 ; E-mail address: egemen.teomete@deu.edu.tr (E. Teomete)
ISSN: 2149-8024 / DOI: https://doi.org/10.20528/cjsmec.2017.02.007

2. Experimental Method

In this study, six different concrete mixes were designed; one without any copper powder, the rest five having different copper powder volume fractions. Three cube samples from each mix were cast and cured. In all mixes, cement Batıçim CEM II/B-M (L-W) 42,5R was used. BASF silica fume/cement was 10%; water/binder was 0.37; super plasticizer Sika ViscoCrete High Tech 30/binder was 1%. The maximum and the minimum diameter of the aggregate was 0-15mm. Two type of aggregate was used in the mix. Fine aggregate size was between 0-5mm and coarse aggregate size was between 5-15mm. Copper powder was examined under the microscope as seen in Fig. 1. The shape of the copper powder is circular and has a maximum diameter of 300 μm. In mix M0, there was not any conductive material. The mixes Cop1, Cop2, Cop3, Cop4 and Cop5 have copper powder volume fractions of 0.2% - 0.35% - 0.5% - 0.8% and 1% respectively.

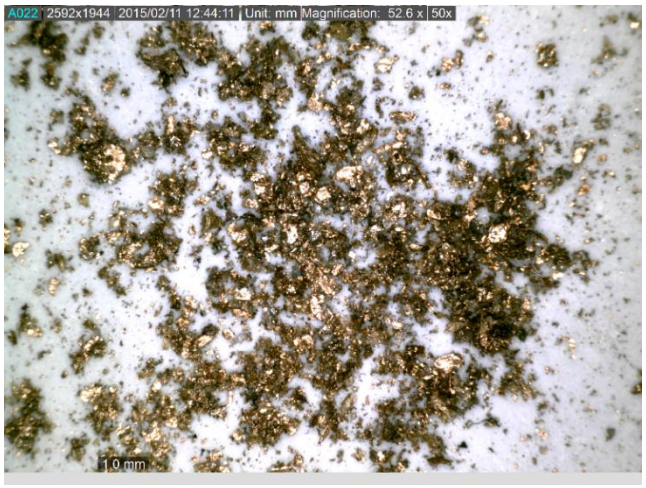

Fig. 1. Copper powder microscope image (magnification: 50x).

Three samples of 7.5 cm cubes were casted for each mix. Special 7.5 cm cube shaped molds were designed and manufactured for this study. The molds have four 2 mm wide, 55 mm long slots on each side. Pure copper wire mesh was passed through the molds as seen in Fig. 2. The mix was cast in the mold as in Fig. 3. The samples were taken out of molds 24 hours later after casting and the samples were cured in water for 28 days. The samples were taken out of water at 28th day and were kept at laboratory environment for 7 days to have steady state moisture content.

The compression test was achieved with a displacement controlled Shimadzu mechanical test machine at a load rate of 0.5mm/min. The total voltage in put to the circuit in Fig. 4 was 20V. While conducting the test, a DC current was supplied by outer electrodes of the sample as in Fig. 4. Four electrode method was used as it gives more accurate results. There was a reference resistance (R_r=1000 Ohm) and an ampere meter (A) which was in series with the sample. The potential difference between voltage electrodes of the sample (E_v) was measured as V_s and the potential difference across the reference resistance was measured as V_r. A strain gage was used to measure the strain of the sample in force direction. The load, the stroke of the loading head, strain gage data, current, potential differences V_s and V_r were recorded at a rate of 10Hz (10 data in a second) during the test. An image of the sample during compression test was given in Fig. 5.

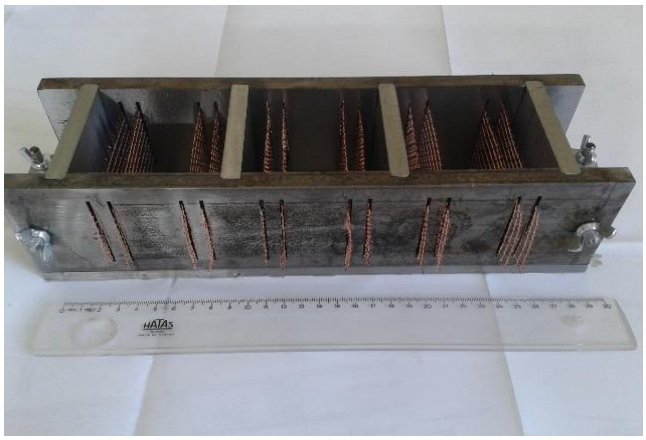

Fig. 2. Mold and copper mesh electrodes.

Fig. 3. Mix casted in mold.

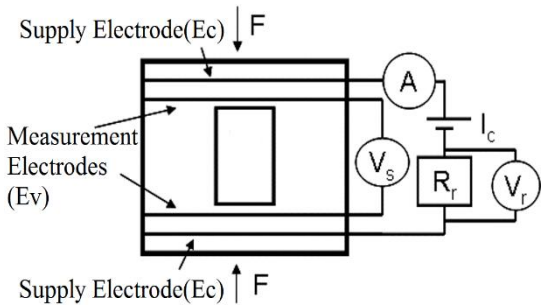

Fig. 4. Circuit diagram used during compression test.

The current on the circuit and the resistance of the sample were determined by using Ohm's law as in Equations 1 and 2. The current determined from Eq. 1 was verified with the ampere meter values. The % change in the resistance of the sample (%R) was determined by Equation 3. R_{so} is electrical resistance of sample without application of any load.

$$I_c = \frac{V_r}{R_r}, \quad (1)$$

$$R_s = \frac{V_s}{I_c}, \quad (2)$$

$$\%R = \left(\frac{R_s}{R_{so}} - 1\right) \times 100\,. \quad (3)$$

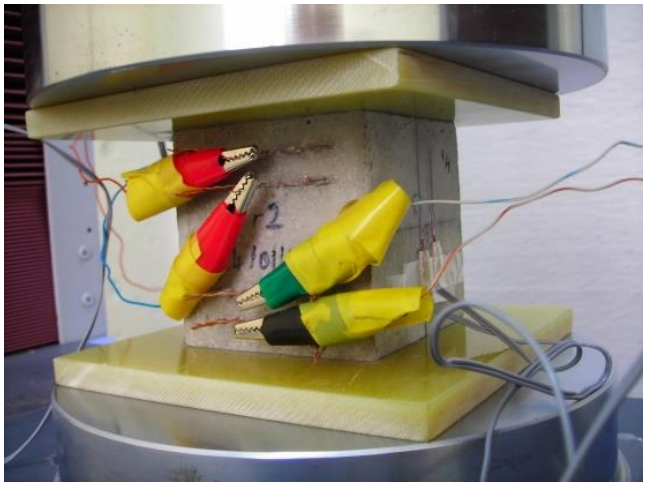

Fig. 5. Compression test.

The gage factor (K), linearity (LE) and strain limit (SL) are performance parameters of a strain gage. Gage factor (K) is the fractional change in electrical resistance per unit strain, and can be determined using Eq. (4). It is a measure of strain sensitivity for strain gages. It is the slope of percent change in resistance ($\%R$) versus strain graph divided by 100. The higher the K, the more sensitive the sensor is. The gage factor of commercial metal strain gages is around 2. Linearity (LE) is the percent of maximum difference (Δ_{max}) between input-output curve ($\%R$ versus strain curve) and fitted linear regression line, to full scale output (R_{fs}), as given in Eq. (5). The error in measurement of strain decreases by decreasing linearity. The strain limit (SL) of a strain gage is the maximum strain that can be measured with a small error. The strain limit (SL) of typical commercial metal strain gage is between 0.005-0.03.

$$K = \frac{(R_s - R_{so})/R_{so}}{\Delta\varepsilon}, \quad (4)$$

$$\%LE = \left(\frac{\Delta_{max}}{\%R_{fs}}\right) \times 100\ . \quad (5)$$

3. Results and Discussion

Six different concrete mixtures were designed; one without any copper powder, the rest five having different copper powder volume fractions. From each mix, three of 7.5 cm cubes were tested with compression test. The relations between compressive strain – electrical resistance change were determined. These results are presented in this section.

The $\%R$ – strain graph of mix M0 is given in Fig. 6. The gage factor of mix M0 which does not have any conductive materials is K=21. It is 10 times more sensitive to strain than metal foil strain gages. It has a linearity of 15% and its strain limit (SL) is 2%. The correlation coefficient of best fit line to the data is 0.93.

The $\%R$ – strain graph of mix Cop1 is given in Fig. 7. The volume fraction of the copper powder in the Cop1 mix is 0.2%. The gage factor is K=41 which is 20 times more sensitive to strain. The linearity is LE=5% and the strain limit is 1.5%. The correlation coefficient of best fit line to the data is 0.99.

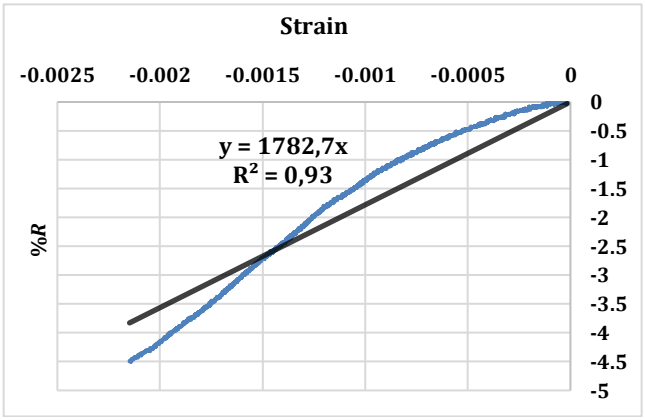

Fig. 6. M0 mixture without conductive (K=21; LE=15%; SL=2%).

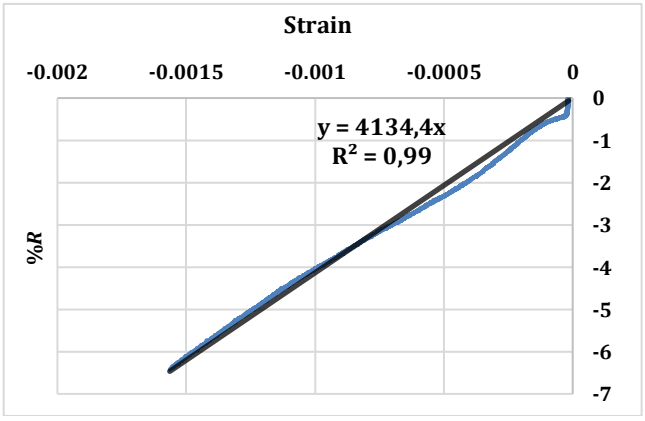

Fig. 7. Cop1 mixture with 0.2% copper powder (K=41; LE=5%; SL=1.5%).

The $\%R$ – strain graph of mix Cop2 is given in Fig. 8. The volume fraction of the copper powder in the Cop2 mix is 0.35%. The gage factor is K=53 which is 26 times more sensitive to strain. The linearity is LE=5% and the strain limit is 1.3%. The correlation coefficient of best fit line to the data is 0.98.

The $\%R$ – strain graph of mix Cop3 is given in Fig. 9. The volume fraction of the copper powder in the Cop3 mix is 0.5%. The gage factor is K=27 which is 13 times more sensitive to strain. The linearity is LE=6% and the strain limit is 2.4%. The correlation coefficient of best fit line to the data is 0.99.

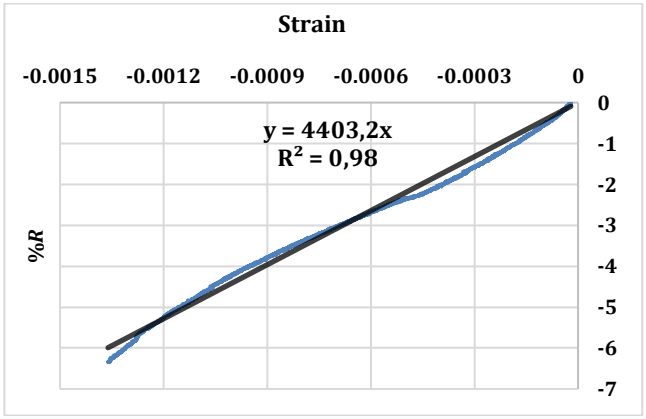

Fig. 8. Cop2 mixture with 0.35% copper powder (*K*=53; *LE*=5%; *SL*=1.3%).

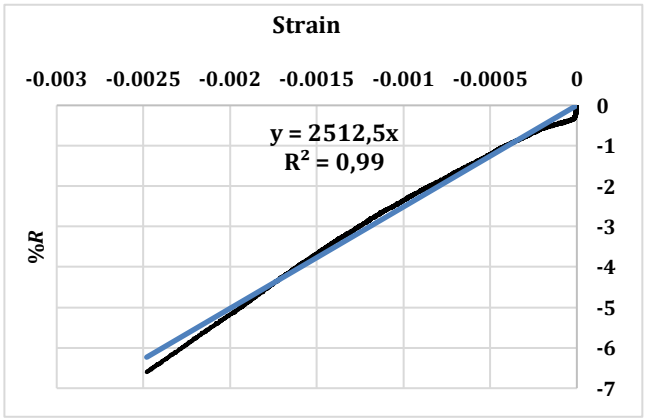

Fig. 9. Cop3 mixture with 0.5% copper powder (*K*=27; *LE*=6%; *SL*=2.4%).

The %*R* – strain graph of mix Cop4 is given in Fig. 10. The volume fraction of the copper powder in the Cop4 mix is 0.8%. The gage factor is *K*=33 which is 8 times more sensitive to strain. The linearity is *LE*=23% and the strain limit is 1.6%. The correlation coefficient of best fit line to the data is 0.94.

The %*R* – strain graph of mix Cop5 is given in Fig. 11. The volume fraction of the copper powder in the Cop5 mix is %1. The gage factor is *K*=38 which is 19 times more sensitive to strain. The linearity is *LE*=10% and the strain limit is 1.8%. The correlation coefficient of best fit line to the data is 0.99.

The gage factor (*K*), linearity (*LE*) and correlation coefficient (R^2) versus copper powder volume percent were given in the Figs. 12-13-14. The Figs. 12-13-14 shows average values of three samples that casted for each group. There are five copper powder reinforced mix groups which have different copper powder volume fractions and there is M0 group which does not have any copper powder.

The gage factor (*K*) – copper powder volume fraction graph of the tested mixes was given in Fig. 12. As seen on the graph all of mixes with copper powder has more gage factor than M0 which does not have any copper powder. Cop2 mix (0.35% copper powder volume fraction) has the highest gage factor in all of the mixes. Cop2 mix has an average of 44 gage factor. This mix was 22 times more sensitive to strain than commercial foil strain gages. The gage factor is decreasing with the increasing copper powder volume fraction. As the copper powder volume percent increased from 0.35% to 1%, strain could disrupt a smaller percent of the conductive-conductive and conductive-matrix contact; the effect of strain on the electrical resistance got smaller; %*R* changed less; strain sensitivity decreased and gage factor decreased.

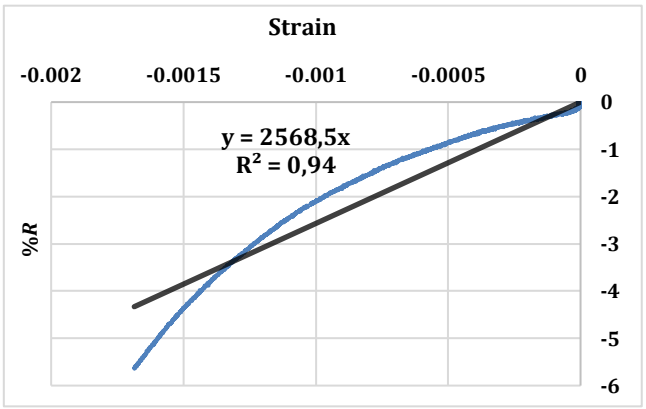

Fig. 10. Cop4 mixture with 0.8% copper powder (*K*=33; *LE*=23%; *SL*=1.6%).

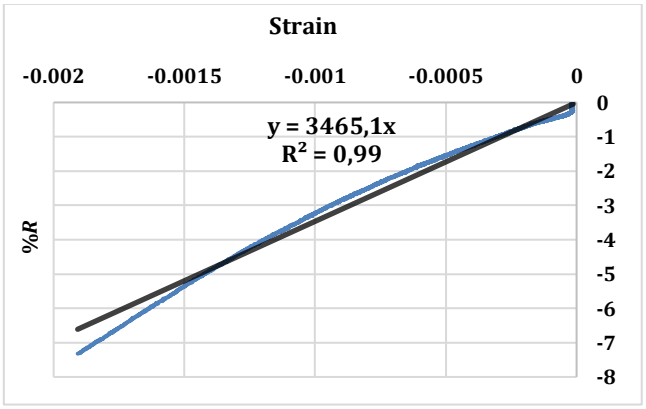

Fig. 11. Cop5 mixture with 1% copper powder (*K*=38; *LE*=10%; *SL*=1.8%).

The linearity (*LE*) – copper powder volume fraction graph of mixes was given in Fig. 13. As seen on the graph all of mixes with copper powder has *LE* deviation than M0 which does not have any copper powder in it. Cop1 (0.2% copper powder volume fraction) and Cop2 (0.35% copper powder volume) have the lowest *LE* in all of the mixes. The average linearity of Cop1 mix is *LE* = 6.79% and the average linearity of Cop2 mix is *LE* = 6.65%. The deviation is increasing with the increasing copper powder volume fraction.

The correlation coefficient (R^2) – copper powder volume fraction graph of mixes was given in Fig. 14. As seen on the graph all of mixes with copper powder had higher correlation coefficient than M0 which did not have any copper powder. The highest correlation coefficient was 0.99 which testified the strong linear relationship between compressive strain and electrical resistance change.

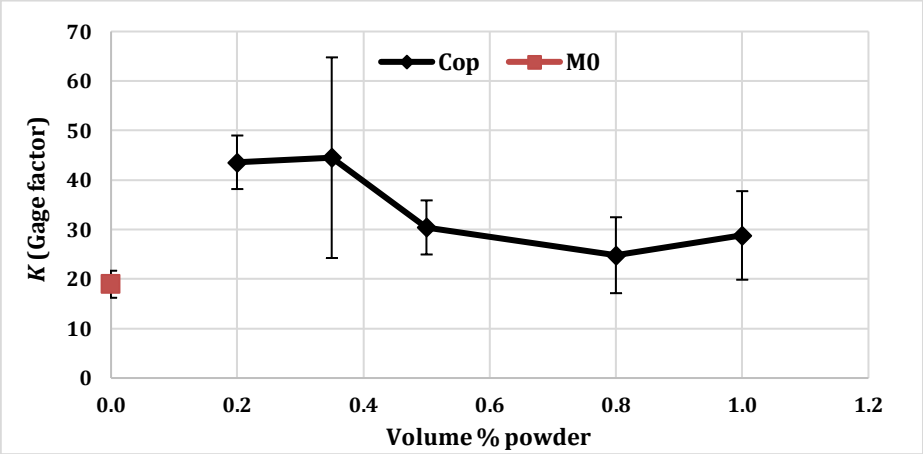

Fig. 12. The gage factor (*K*) vs. copper powder volume fraction graph of mixes.

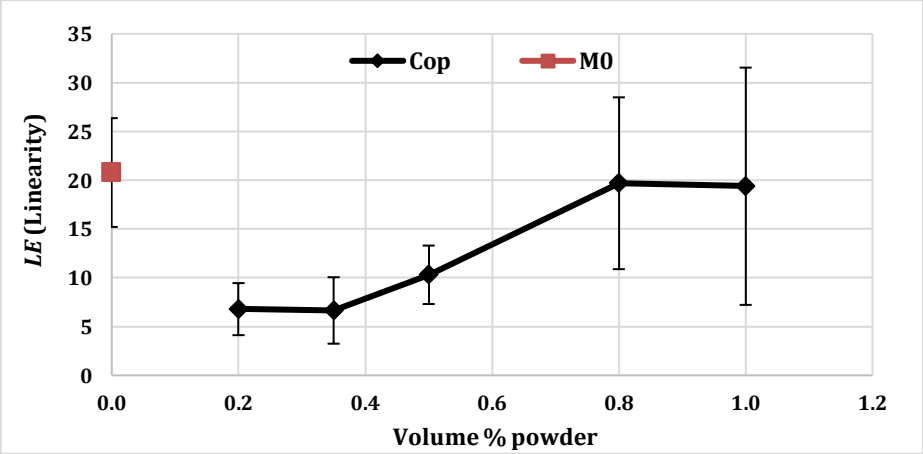

Fig. 13. The Linearity (*LE*) vs. copper powder volume fraction graph of mixes.

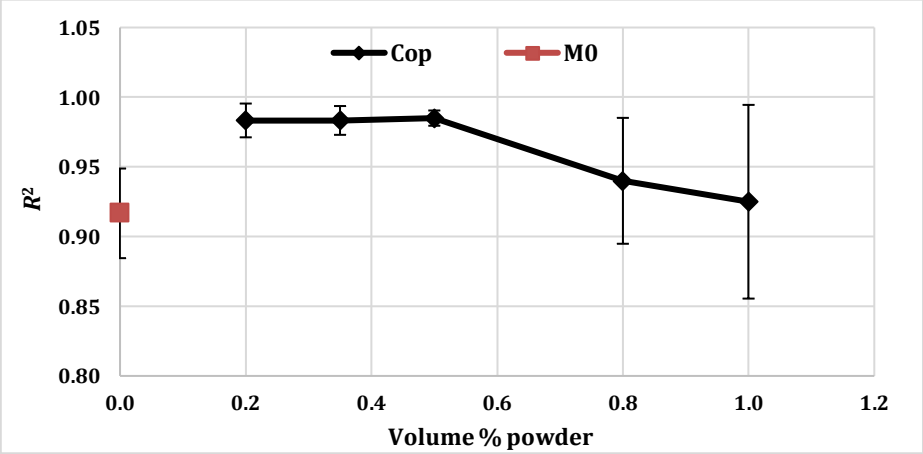

Fig. 14. The correlation coefficient (R^2) vs. copper powder volume fraction graph of mixes.

4. Conclusions

Five different samples with different copper powder volume fractions and one sample without any copper powder in it were tested in this study. Simultaneous measurement of sample resistance and strain were recorded. It was observed that:

- The compressive strain closed micro cracks and voids, increased contact between concrete matrix-copper powder, powder- powder and resulted in a decrease in the electrical resistance.
- There was a strong linear relationship between compressive strain and electrical resistance change. An average gage factor of 44 was obtained which was the

almost 20 times the gage factor of commercial metal foil strain gages.
- Copper powder reinforced concrete was more sensitive to strain and had better signal than plain concrete.
- The copper powder reinforced concrete composites were much more sensitive to strain with respect to commercial metal strain gages.
- At low volume fractions (0.2% and 0.35%), copper powder reinforced concrete had a high gage factor and a better signal quality with respect to other volume fractions.

The results are contribution to the development of "Smart Concrete" which can sense its strain and damage.

Acknowledgements

This work is supported by The Scientific and Technological Research Council of Turkey (TUBITAK) through Grant no: 213M452. The authors would like to thank to Batıbeton Batıçim West Anatolia Cement Industry Inc. for supplying cement and aggregate; Sika Construction Chemicals Co. for supplying super plasticizer; BASF Chemical Co. for supplying silica fume, BMS Metal Inc. for supplying copper fibers.

References

Chen B, Liu J (2008). Damage in carbon fiber –reinforced concrete, monitored by both electrical resistance measurement and acoustic emission analysis. *Construction and Building Materials*, 22, 2196-2201.

Chiarello M, Zinno R (2005). Electrical conductivity of self-monitoring CFRC. *Cement and Concrete Composites,* 27, 463-469.

Chung DDL (1998). Self-monitoring structural materials. *Materials Science Engineering,* 22(2), 57-78.

Chung DDL (2000). Cement reinforced with short carbon fibers: a multifunctional material. *Composites Part B: Engineering,* 31, 511-526

Chung DDL (2001). Review functional properties of cement –matrix composites. *Journal of Materials Science,* 36, 1315-1324.

Fu X, Ma E, Chung DDL, Anderson WA (1997). Self-monitoring in carbon fiber reinforced mortar by reactance measurement. *Cement and Concrete Research,* 27(6), 845-852.

Han B, Guan X, Ou J (2007). Electrode design, measuring method and data acquisition system of carbon fiber cement paste piezoresistive sensors. *Sensors and Actuators A,* 135, 360-369.

Reza F, Baston GB, Yamamuro JA, Lee JS (2003). Resistance changes during compression of carbon fiber cement composites. *Journal of Materials in Civil Engineering*, 15(5), 476-483.

Reza F, Yamamuro YA, Baston GB (2004). Electrical resistance change in compact tension specimens of carbon fiber cement composites. *Cement and Concrete Composites,* 26, 873-881.

Teomete E (2015). Measurement of crack length sensitivity and strain gage factor of carbon fiber reinforced cement matrix composites. *Measurement*, 74, 21-30.

Challenge Journal of Structural Mechanics

Elastic foundation effects on arch dams

Muhammet Karabulut *, Murat Emre Kartal, Omer Faruk Capar, Murat Cavusli

Department of Civil Engineering, Bülent Ecevit University, 67100 Zonguldak, Turkey

ABSTRACT

Earthquake response of an arch dam should be calculated under ground motion effects. This study presents three-dimensional linear earthquake response of an arch dam. Thereby, we considered different ground motion effects and also foundation conditions in the finite element analyses. For this purpose, the Type 3 double curvature arch dam was selected for application. All numerical analyses are carried out by SAP2000 program for empty reservoir cases. In the scope of this study, linear modal time-history analyses are performed using three dimensional finite element model of the arch dam and arch dam-foundation interaction systems. According to numerical analyses, maximum horizontal displacements and maximum normal stresses are presented by dam height in the largest section. These results are evaluated for rigid and various elastic foundation conditions. Furthermore, near-fault and far-field ground motion effects on the selected arch dam are taken into account by different accelerograms obtained from the Loma Prieta earthquake at various distances.

ARTICLE INFO

Article history:
Received 2 February 2017
Accepted 25 February 2017

Keywords:
Elastic foundation
Far-field ground motion
Near-fault ground motion
Type 3 arch dam

1. Introduction

Arch dam construction is the most difficult type because of its geometrical shape design. The arch dam bodies transmit the load of reservoir water pressure and partially weight of dam body to valley. Therefore, these dam type requires more sophisticated engineering than other dam types. Despite the fact that dam failures are rare, a number of factors including age, construction deficiencies, inadequate maintenance and weather or seismic events contribute to the possibility of a dam's failure (Mosallam and Banerjee, 2007; Mirzaei et al., 2010). Besides, empty reservoir conditions should be investigated especially for arch dams. The arch dams design in order to hold huge water pressure behind them. We study that what happens in empty reservoir conditions and how the dam's behavior changes under earthquake.

Rigorous analysis of concrete arch dam–reservoir systems is based on the finite element method. This means, the dam is discretized by solid finite elements. In our country, dams which have been built up until now, consist of approximately 75% earthfill dams, 17% rockfill dams and only 2% arch dams (Calamak et al., 2013). Arch dams have thinner sections than compare with concrete gravity dams and it causes saving concrete. Generally, arch thickness has to be smaller than 60% height of arch. When the thickness of arch section rises, arch gravity and concrete gravity dam must be considered. Constructing of an arch dam is more beneficial to produce water energy if there is a suit region to build an arch dam. However, arch dam has some disadvantages such as analyses and design process. Besides, the qualification of the slope process must be carried out very carefully. Valley must have high bearing capacity for foundation and also slopes to construct an arch dam.

In this study, we investigated the effect of the elastic foundation conditions on the response of the Type 3 arch dam which is one of the three type models proposed in Arch Dams Symposium organized in England (Dennis, 1968). For this purpose, we designed three finite element models. All models compose of dam body and foundation soil. We analyzed these three models under near-fault and far-field ground motion effects.

According to numerical analyses, horizontal displacements and maximum normal stresses are calculated and evaluated for the elastic foundation conditions. Some parameters are crucially important on stresses such as modulus of elasticity, Poisson's ratio and cohesion value.

* *Corresponding author*. Tel.: +90-537-9859663 ; Fax: +90-372-2514023 ; E-mail address: karabulut@beun.edu.tr (M. Karabulut)
ISSN: 2149-8024 / DOI: https://doi.org/10.20528/cjsmec.2017.02.006

If soil elasticity value changes, maximum stress and displacement changes. It is clear that soil elasticity value increases, maximum stress and horizontal displacement decrease. Besides, ratio of concrete elasticity of dam body and soil elasticity (E_c/E_f) should be lower than 4 especially for arch dams.

2. Effect of Near Fault and Far Field Ground Motion

Ground motions produced from earthquakes differ from one another in characteristics, distance, magnitude and direction from the rupture location and local soil conditions. The effects of near fault and far field ground motion on civil engineering structures such as bridges, tunnels, buildings and dams have been the subject of recent studies but they are not enough. A number of investigators have studied the effect of near fault-far field ground motion on the seismic behavior of dams and all of them are agree that the effect of near-fault ground motion is vital importance (Davoodib et al., 2013). It can be clearly seen from this study that the importance of near-fault and far field ground motion effects on the linear dynamic response of structures has been highlighted. The unique characteristics of the near-fault ground motions can lead to significant damage during an earthquake. It was taken into account by different accelerograms obtained from the Loma Prieta earthquake at various distances. The distance for near-fault effect is 5.1 km and it is 93.1 km for far-field effect. The north-south, east-west and vertical (x, y and z) directions of accelerograms of Loma Prieta were used in numerical analyses.

3. Mathematical Model of Type 3 Arch Dam

In this study, finite element method was used for modelling and analyses. Dam body was divided to 204 eight-noded solid finite elements. This study presents linear modal time-history analyses of dam-foundation interaction systems. We selected different elastic foundation conditions.

The height of the dam is selected as 120 m. The depth of the foundation is taken into consideration as the dam height. Three dimensional finite element model of Type 3 dam includes eight-noded finite elements. These elements have three degree of freedom in every nodal point as displacements of directions x, y and z. Three dimensional finite element model of the arch dam has 263 nodal points and 204 number of solid elements. Arch components of dam are assumed as monolithic, homogeny and isotropic in linear modal time-history analyses under ground motion effects. Contraction joints between concrete blocks were ignored. The finite element models are presented in Fig. 1(a, b).

Dam foundation dimension size must be at least one or two times of dam height provides sufficient approach on downstream and upstream parts of dam. If one should want to obtain reservoir water effects, the upstream side should be at least three times of the dam height. The fixed boundary conditions were used for foundation rock in the finite element model.

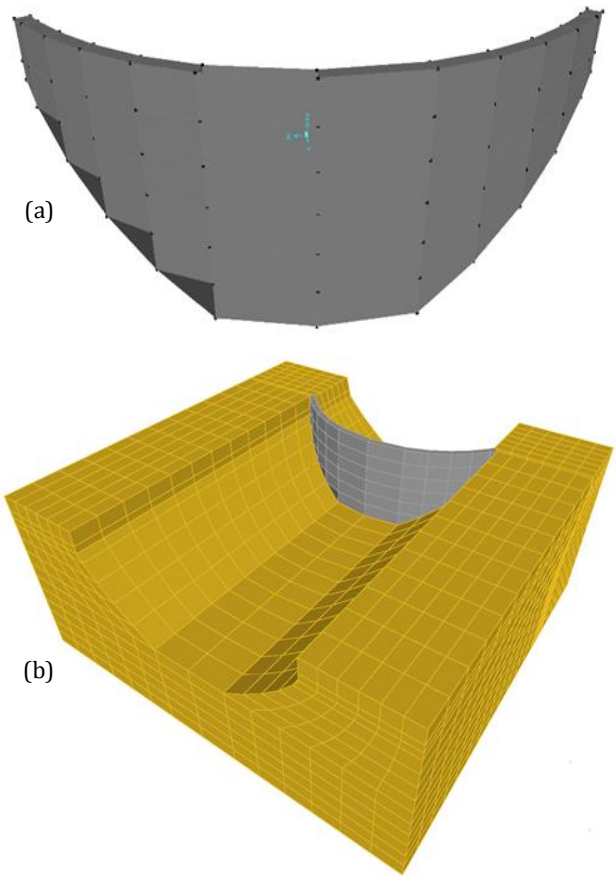

Fig. 1. Finite element model of: (a) arch dam body; (b) arch dam-foundation interaction.

Table 1. Material properties of concrete arch dam body and foundation.

Models	Colors	Modulus of Elasticity E (kN/m²)	Compressive Strength (kN/m²)	Poisson's Ratio ν
Dam Body	Grey	32000000	30000	0.20
Model 1	Blue	8200000	9389	0.25
Model 2	Green	14064000	18084	0.25

All different soil conditions models include fixed boundary condition in the edge of the foundation. Material properties of elastic foundations was calculated by means of the Hoek-Brown failure criterion for rock masses (Hoek et al., 2002). Their semi-theoretical approach is extensively acknowledged to produce input data for rock-mechanic analyses. The Hoek–Brown approach using Geological Strength Index (GSI) is widely

used for assessing stiffness and shear strength parameters. The values of GSI change between 55 and 75. The minimum GSI value picked 55 for the foundation of Model 1. Model 2 GSI value picked 65 and then Model 3 GSI value picked 75. The non-linear Hoek-Brown Failure criterion is

$$\sigma_1' = \sigma_3' + \sigma_{ci}' \times \left(m_b \times \frac{\sigma_3'}{\sigma_{ci}'} + s \right)^a , \quad (1)$$

$$m_b = m_i \times e^{\left(\frac{GSI-100}{28-14\times D}\right)} v = \sqrt{\left(\frac{V_n - V_p}{bd_v}\right)^2 + \left(\frac{T_n}{1.7A_{oh}t_w}\right)^2} , \quad (2)$$

$$s = e^{\left(\frac{GSI-100}{28-14\times D}\right)} , \quad (3)$$

$$a = \frac{1}{2} + \frac{1}{6} \times \left(e^{\frac{-GSI}{15}} - e^{\frac{-20}{3}} \right) , \quad (4)$$

where σ_1' and σ_3' are the major and minor effective principal stresses at failure. m_b is reduced value of m_i which is a constant and also function of rock type. σ_{ci} is uniaxial compressive strength of the intact rock. s and a are constants of the rock. D is the disturbance factor influenced by excavation, stress relaxation and blasting (Romana, 2003).

Foundation material was chosen as sand stone. Typical uniaxial compressive strength (σ_{ci}) values of sand stone, as suggested by Hudson (Hudson, 1989), are in the range of 25–175 MPa. It is suggested that typical values of m_i are 17±4 for sandstone. s and a are the constants of rock. D is disturbance factor which permits for the severe effects and stress relaxation. D can be forecast according to guidelines given for several constructions, however not for dams. Because of D is very low for excavations of dam foundations, it cannot be '0' due to decompression. D can be classified as follows:

- Good rock condition D=0.4
- Normal rock condition D=0.2
- Bad rock condition D=0.2

In this study, mechanical excavation was considered for the foundation construction; therefore, D was chosen as 0.4 (Romana, 2003).

These parameters and Eq. (5) were used to determine the modulus of elasticity (E_{rm}) of sandstone material (Hoek and Diederichs, 2006). Finally, determining foundation E_{rm} depends on a formulas:

$$E_{rm}(\text{GPa}) = E_i \times (0.002 + \frac{1-D/2}{1+e^{\left(\frac{(60+15\times D-GSI)}{11}\right)}} . \quad (5)$$

4. Influence of the Elasticity Ratio on the Dam Behavior (E_c/E_f)

Dam engineers consent on which two cases. The situations are dangerous for the behavior of an arch dams: if E_f (foundation deformation modulus) diverges majorly across dam foundation, and other case is that E_c/E_f attains values (E_c is the concrete deformation modulus).

If E_c/E_f value is lower than 4, there is no problem on dams. The minimum value of E_f should be around 5 GPa for a dam. When E_f is less 5 GPa, there happens serious troubles (fracture included) due to the low value of E_f (Romana, 2003).

In this study, we have three different E_c/E_f ratios. Every case has a different E_c/E_f value. It was investigated that how the stresses and displacements change by E_c/E_f value. The numerical analysis results were compared each other. The E_c/E_f ratios change between 1.6 and 3.9 for three different models.

5. Dynamic Analysis

The ground motion effects on the arch dam are considered with east-west, north-south and vertical components of the Loma Prieta earthquake record. 5% damping ratio was used in calculations for the dam-foundation interaction systems. The numerical analyses were realized during 30 seconds. Besides, 0.01 second was selected as the time step.

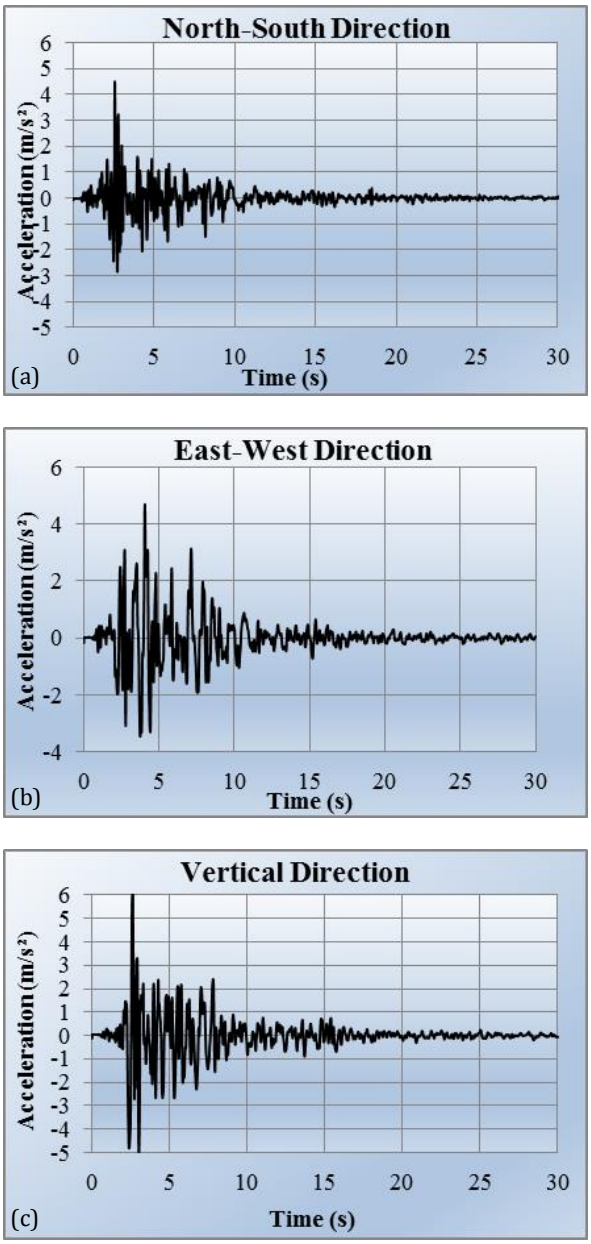

Fig. 2. Accelerogram of Loma Prieta Earthquake for near-fault effect: (a) north-south; (b) east-west; (c) vertical component.

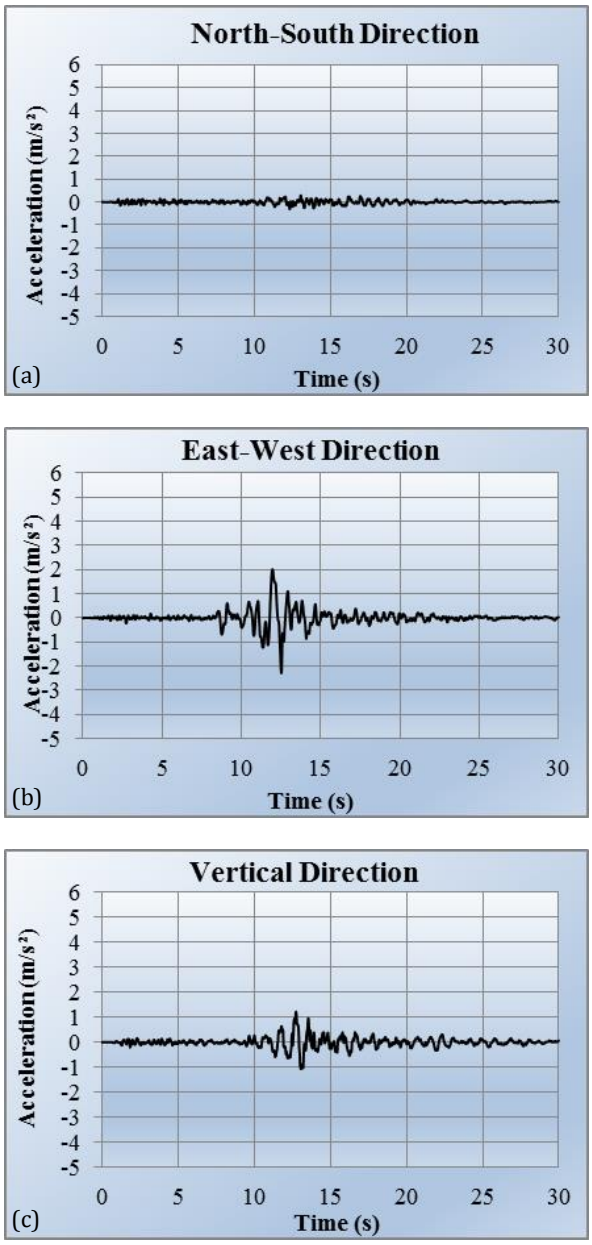

Fig. 3. Accelerogram of Loma Prieta Earthquake for far-field effect: (a) north-south; (b) east-west; (c) vertical component.

The analysis was performed for empty reservoir situation. Rayleigh damping is considered in the solutions with (α, β) constants (Table 2).

According to numerical solutions, it was seen that near-fault ground motions are more effective than far-field for three models. This case was observed in all different numerical models. Such as, maximum displacements were obtained from the model subjected to near-fault earthquake records in linear modal time history analyses. The maximum displacement is 18.9 cm and occurred at upstream direction. The maximum normal stresses occurred at arch direction of the arch dam model and the maximum normal stress is 9074 kPa. All dynamic analysis results show the Model 3 involves lower stress and displacements. Because, Model 3 has bigger modulus of elasticity than the others. In addition, the maximum displacements occurred in Model 1 due to the lower elasticity modulus value. Besides, it is obvious that the distances of the fault have an important role in sizableness of stresses and displacements.

Table 2. Rayleigh damping constants (α, β).

Models	Rayleigh damping constant (α)	Rayleigh damping constant (β)
Model 1	1.15983	0.00189452
Model 2	1.28314	0.00168853
Model 3	1.35167	0.00158081

6. Conclusions

In this study, an arch dam was modeled by SAP2000 software. The arch dam body was composed with solid elements. Then, soils having different modulus of elasticities were modeled. After that the material parameters were assigned. Finite element method was used for solution in SAP2000 software. Loma Prieta earthquake at various distances records were selected to application on dam body and foundation models. Different faults records were used for dynamic linear analysis on three directions. Changing effects of E_c/E_f ratio on the maximum and minimum normal stresses of dam body was investigated.

According to linear modal time-history analysis, the material properties of the foundation affects dam behavior obviously. In addition, different fault distances could be taken into consideration according to the locations of the dam and faults. Therefore, dam-foundation interaction must be considered in dynamic analyses. The foundation of the dam may include various soil materials. The followings can be deducted from this study:

- Maximum displacements were obtained for near-fault effects,
- Maximum displacements obtained in upstream direction,
- Maximum normal stresses occurred at arch direction
- The stresses and displacements for the Model 3 are lower than those including different elasticity modulus of foundation conditions,
- If the modulus of elasticity of dam foundation increases, the stresses and displacements of the dam decrease.
- E_c/E_f is an important factor for the selected dam type in the construction location.

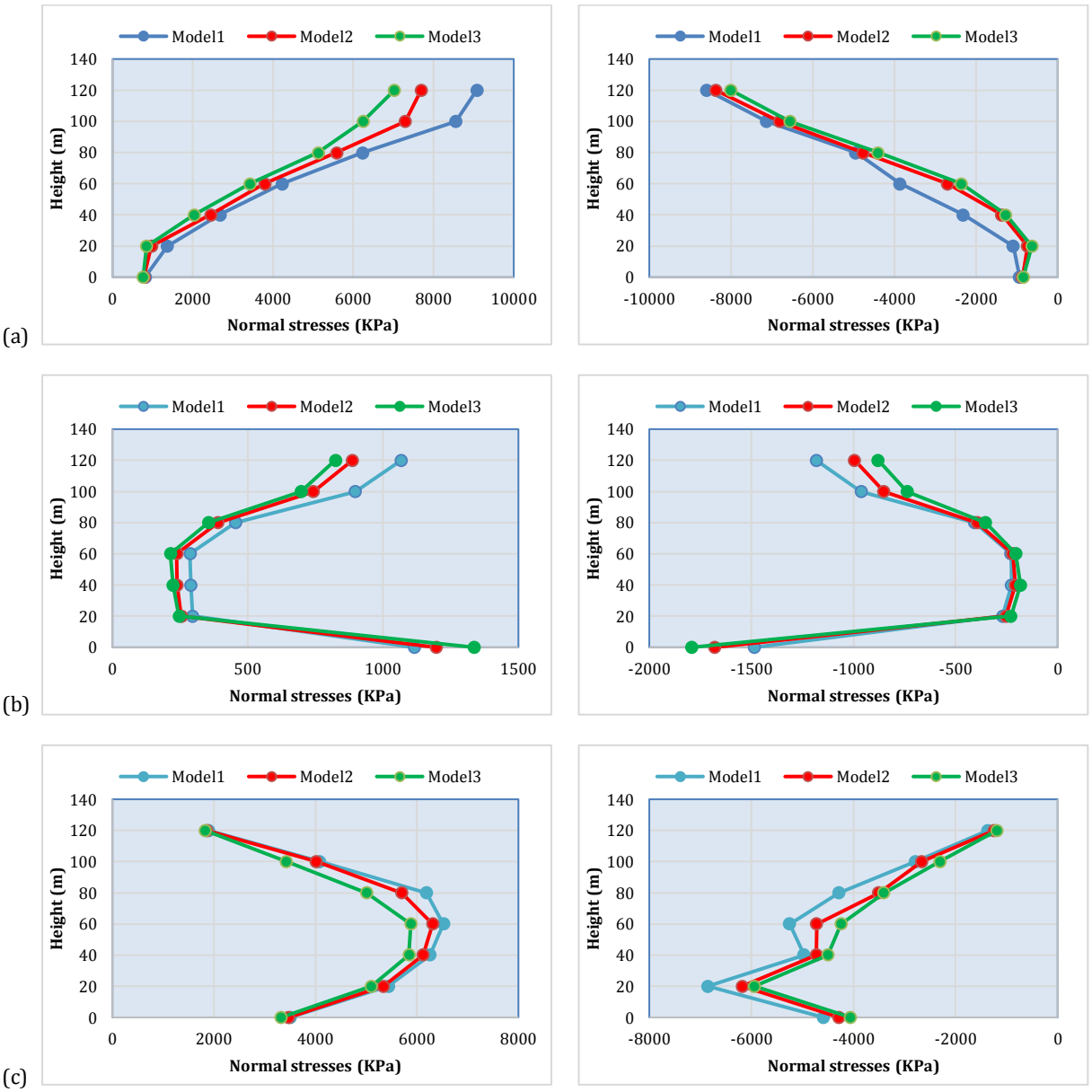

Fig. 4. Maximum and minimum normal stresses at each direction for near-fault ground motion effect: (a) *x* direction; (b) *y* direction; (c) *z* direction.

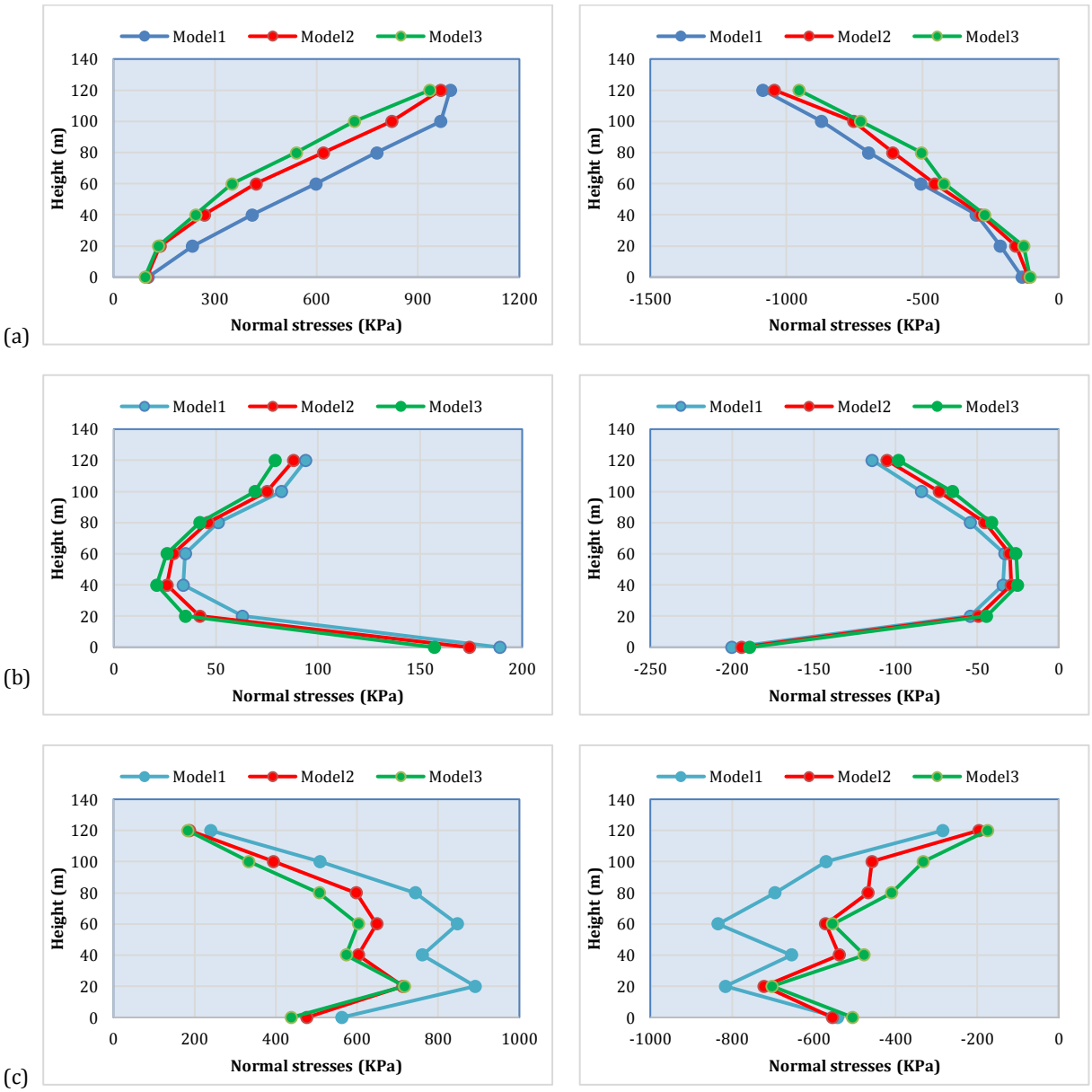

Fig. 5. Maximum and minimum normal stresses at each direction for far field ground motion effect: (a) *x* direction; (b) *y* direction; (c) *z* direction.

REFERENCES

Calamak M, Arıcı Y, Yanmaz AM (2013). An evaluation on the development on dam engineering in Turkey. Department of Civil Engineering, METU, Çankaya, Ankara, December (in Turkish).

Davoodib M, Jafarib MK, Hadiani N (2013) Seismic response of embankment dams under near-fault and far-field ground motion excitation. *Engineering Geology*, 158, 66–76.

Dennis TL (1968). Arch Dams: A review of British research and development. *Proceedings of the Symposium Held at the Institution of Civil Engineers*, London, England.

Gercek H (2007). Poisson's ratio values for rocks. *International Journal of Rock Mechanics & Mining Sciences*, 44, 1–13, Zonguldak, Turkey

Hoek E, Carranza-Torres C, Corkum B (2002). Hoek-Brown Failure Criterion – 2002 Edition. *5th North American Rock Mechanics Symposium and 17th Tunneling Association of Canada Conference: NARMS-TAC*, 267-271.

Hoek E, Diederichs MS (2006). Empirical estimation of rock mass modulus. *International Journal of Rock Mechanics and Mining Sciences*, 43(2), 203-215.

Hudson JA (1989). Rock Mechanics Principles in Engineering Practice. Butterworths, London

Mirzaei E, Vahdani S, Mirghaderi R (2010). Seismic analysis of double curved arch dams based performance. *Proceedings of the World Congress on Engineering and Computer Science (WCECS)*, 2, San Francisco, USA.

Mosallam AS, Banerjee S (2007). Shear enhancement of reinforced concrete beams strengthened with FRP composite laminates. *Composites: Part B*, 38(5-6), 781–93.

Romana M (2003). DMR (Dam Mass Rating): An adaptation of RMR geomechanics classification for use in dams foundations. *10th ISRM Congress*, Sandton, South Africa.